PCCP

Multivalent optical cycling centers: towards control of polyatomics with multi-electron degrees of freedom

Journal:	*Physical Chemistry Chemical Physics*
Manuscript ID	CP-ART-08-2022-003545.R1
Article Type:	Paper
Date Submitted by the Author:	11-Nov-2022

Complete List of Authors:	Yu, Phelan; California Institute of Technology, Division of Physics, Mathematics, and Astronomy Lopez, Adrian; California Institute of Technology, Division of Physics, Mathematics, and Astronomy Goddard III, William; California Institute of Technology, Division of Chemistry and Chemical Engineering Hutzler, Nicholas; California Institute of Technology, Division of Physics, Mathematics, and Astronomy

PCCP

ARTICLE TYPE

Cite this: DOI: 00.0000/xxxxxxxxxx

Multivalent optical cycling centers: towards control of polyatomics with multi-electron degrees of freedom†

Phelan Yu*[a], Adrian Lopez[a‡], William A. Goddard III[b], and Nicholas R. Hutzler[a]

Received Date
Accepted Date

DOI: 00.0000/xxxxxxxxxx

Optical control of polyatomic molecules promises new opportunities in precision metrology and fundamental chemistry, as well as quantum information and many-body science. Contemporary experimental and theoretical efforts have mostly focused on cycling photons via excitation of a single electron localized to an alkaline earth (group 2)-like metal center. In this manuscript, we consider pathways towards optical cycling in polyatomic molecules with multi-electron degrees of freedom, which arise from two or more cycling electrons localized to *p*-block post-transition metal and metalloid (group 13, 14, and 15) centers. We characterize the electronic structure and rovibrational branching of several prototypical candidates using *ab initio* quantum chemical methods. Despite increased internal complexity and challenging design parameters, we find several molecules possessing quasi-closed photon cycling schemes with highly diagonal, visible and near-infrared transitions. Furthermore, we identify new heuristics for engineering optically controllable and laser-coolable polyatomic molecules with multi-electron cycling centers. Our results help elucidate the interplay between hybridization, repulsion, and ionicity in optically active species and provide new directions for using polyatomic molecules with complex electronic structure as a resource for quantum science and measurement.

Cold molecules are powerful platforms for exploring a range of fundamental questions in physics and chemistry. Unique mechanical, spin, and dipolar degrees of freedom available in molecules enable new possibilities in quantum information[1–4] and many-body simulation[5–7], precision measurement and metrology[8,9], as well as state-resolved chemistry[10–12]. In the last five years, laser cooling and optical control have been extended to increasingly complex polyatomic molecules, paving the way towards the high phase space density[13,14] and coherent quantum control[15–17] necessary for realizing science applications with cold gases of optically active polyatomic molecules. Simultaneously, theoretical understanding of the features that make molecules amenable to optical cycling and laser cooling has significantly advanced[18–29], leading to the identification of several classes of polyatomics with favorable chemical and structural configurations.

A key characteristic of photon cycling in molecules is the presence of valence electrons localized to metallic optical cycling centers (OCCs), which enable rapid, repeated scattering of resonant photons for optical state control, detection, and cooling. The simplest "monovalent" OCCs can be engineered by bonding an alkaline earth-like (AEL) metal[§] to a one-electron acceptor or pseudohalogen ligand[18,19,30–32], forming an open-shell molecule (e.g. SrF[33–37], CaF[13,15,38–40], YbF[41,42], BaH[43], BaF[44,45]) with an excited electronic structure roughly similar to alkali atoms. The remaining $s\sigma$ electron on the metal is then polarized away from the ionic metal-ligand bond. Metal-centered, atom-like electronic excitations are highly decoupled from the rovibrational modes of the molecule, with only a handful of repumping lasers needed to scatter $10^3 - 10^5$ photons[18,26,46–48]. This heuristic has been very successful at identifying laser-coolable molecules, and all polyatomic species laser cooled to date (SrOH[49], CaOH[50,51], YbOH[52], $CaOCH_3$[53]) have followed the AEL-pseudohalogen template to form single electron, alkali-like OCCs.

A natural question then follows: is it possible to design molecules containing optical centers with *multiple* localized cycling electrons, while preserving key structural features that enable optical control and laser cooling? In cold atom experiments,

[a] *Division of Physics, Mathematics, and Astronomy, California Institute of Technology, Pasadena, California 91125, USA.*
[b] *Division of Chemistry and Chemical Engineering, California Institute of Technology, Pasadena, California 91125, USA.*
‡ *Present address: Harvard-MIT Center for Ultracold Atoms, Cambridge, Massachusetts 02138, USA*
* Email: phelanyu@caltech.edu

† Electronic Supplementary Information (ESI) available: Detailed discussion on the electronic structure of multivalent OCCs, including additional details on molecular orbital and valence bond descriptions of each OCC class, as well as information on the rotational structure and selection rules for optical cycling. Also included are the tabulated outputs of the EOM-CC calculations (energies, geometries, transition dipole moments, and spin-orbit couplings) and electron population analyses. See DOI: 10.1039/cXCP00000x/

§ This includes alkaline earths (Be, Mg, Ca, Sr, Ba, Ra) and transition metals with s^2 valence and filled d/f-shells (e.g. Yb, Hg)

multi-electron degrees of freedom provide versatile mechanisms for both controlling and studying the behavior of complex quantum systems. Individual atoms that possess two (or more) valence cycling electrons, such as AEL atoms, give rise to electronic states with metastable lifetimes[54,55], ultranarrow optical transitions[56–58], perturbation-free "magic" trapping conditions[59–61], efficient autoionization pathways[62–64], and fully tunable couplings to internal spins[65].

Leveraging these features in multi-electron atoms has been a principal factor enabling record-setting optical lattice[66–69] and tweezer clocks[70,71], analog many-body simulators of high-dimensional and multiorbital Hamiltonians[72–77], advanced atom interferometers[78], high-fidelity entangling gates[64,79,80], and telecom-compatible quantum transducers and memories[81–85].

In this manuscript, we assess the feasibility of using generalized, "multivalent" electronic structure for photon cycling and optical control of polyatomic molecules. For the purposes of this manuscript, we define "multivalent" as describing systems with multiple valence electrons localized on the molecular OCC, in contrast to "monovalent" systems with a single OCC-localized valence electron. We find that the bonding paradigms needed to engineer multivalent OCCs in polyatomic molecules are significantly different from the structural features previously used to design monovalent candidates. Our resulting approach is, to our knowledge, the first molecular design for polyatomic OCCs that emphasizes orbital repulsion and covalency, rather than bond ionicity and atom-like features, to achieve quasi-closed cycling transitions.

As proof-of-principle, we theoretically examine polyatomic molecules functionalized with *p*-block elements from group 13, 14, and 15 of the periodic table, such as Al. Experimental studies have already found diatomic analogs, namely AlF[86,87], AlCl[88], and TlF[89,90], to be excellent laser cooling candidates, and theoretical work has identified around a dozen other promising species composed of *p*-block elements bonded to a halogen atom[91–97,97–101]. Functionalizing larger, polyatomic molecules with multivalent OCCs would combine previously heterogeneous features in a single molecule: 1) clock-state metrology and multi-electron degrees of freedom and 2) custom internal structure from the molecular ligand, which can yield long-lived, highly polarizable states[8,102], tunable long-range interactions[3,103,104], and built-in co-magnetometers[8,9]. However, the bonding paradigms which work to create cycling centers on monovalent AEL-type OCCs, such as substituting a halogen for a hydroxide[9,18,19,22,105], do not apply to these new systems. For example, AlF has a structure which is highly amenable to photon cycling[86,87], while AlOH does not (see Sec. 3).

Thus, we must devise alternative approaches for identifying species which combine the advantages of polyatomic structure with multivalent cycling centers. By choosing a linker atom which creates a more covalent metal-ligand bond than oxygen (such as sulfur) we find that molecular vibrations are decoupled from the valence OCC electrons through an intricate interplay of orbital hybridization, ionicity, and repulsion. We eluciate these orbital mechanisms for a variety of OCCs and ligands in order to gain insight into their effects on the internal structure and photon cycling in our candidate systems. These results in turn enable us to deduce new bonding principles and optimal linker atom architectures for engineering optically controllable polyatomic molecules with complex electronic structure.

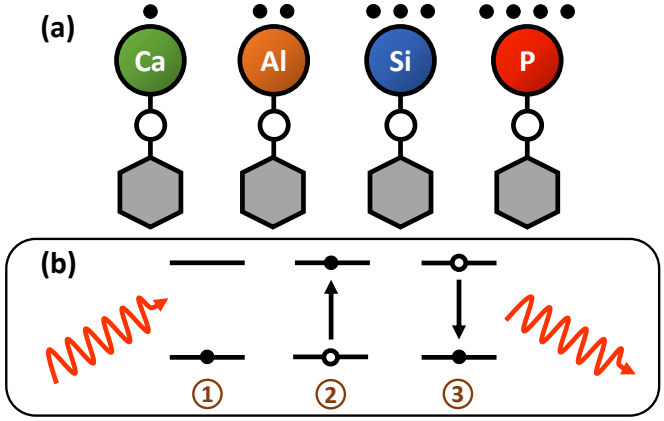

Fig. 1 (a) Lewis dot structures depicting model "monovalent" and "multivalent" polyatomics with metal and metalloid optical cycling centers bonded to a pseudohalogen ligand. (b) Photon cycling in an idealized two-level system proceeds via the (1) absorption of a resonant photon, (2) followed by a transition to an excited electronic state. After the excited state lifetime elapses, (3) the excited state decays, releasing a photon through spontaneous emission.

The model systems we characterize are of the form M*X*H, where M is a group 13, 14, or 15 atom and *X* is a chalcogen (*X* = O, S, Se, Te, Po) linker atom. Despite their increased structural complexity and challenging design constraints, our theoretical analysis predicts that several of these polyatomic molecules have highly decoupled, visible wavelength and near-infrared electronic transitions that support quasi-closed photon cycling schemes. For each class of polyatomics, we find species with diagonal Franck-Condon behavior, which in some cases, may enable photon cycling schemes that are quasi-closed up to one-part-in-10^5.

1 Pathways to Photon Cycling

During photon cycling, valence electrons hosted by metallic OCCs undergo rapid cycles of coherent absorption and spontaneous emission of photons[30–32], which can enable efficient optical state preparation, as well as high-fidelity detection and control. The resulting momentum transfer, in analogy to atomic laser cooling[106], can also facilitate slowing, cooling, and trapping of the entire molecule. Building molecules with properties amenable to cycling, however, is a challenging task. For instance, complex rovibrational structures in polyatomic molecules can serve as "dark states" that interrupt an otherwise idealized two-level system for photon cycling. Indeed, laser-coolable molecules follow a strict set of requirements on their internal structure[18,46,48], which include 1) intense visible or near-visible electronic transitions for photon cycling, 2) highly diagonal rovibrational decays and Franck-Condon factors, and 3) the absence of perturbing electronic states in the photon cycling pathway.

Establishing a highly closed photon cycling scheme requires detailed knowledge of transition energies and intensities between the cycling states and possible decay pathways to rovibrational

dark states. Structural relaxation that accompanies spontaneous emission, in particular, will induce branching to vibrational substates, requiring additional re-pump lasers to restore population in the vibrationless cycling states. Most small, optically active molecules – especially of low symmetry – have vibronic wavefunctions that are separable under the Born-Oppenheimer approximation (i.e. the vibrational wavefunction can be expressed as independent of the electronic coordinates). Vibrational decays can therefore be predicted to high accuracy by computing Franck-Condon factors (FCF), which are defined as the overlap integral between vibrational wavefunctions $\psi_{v'}$, $\psi_{v''}$:

$$q_{v',v''} = \left| \int \psi_{v'}(\mathbf{Q}')\psi_{v''}(\mathbf{Q}'')d\mathbf{Q} \right|^2 . \quad (1)$$

Here, v', v'' are the vibrational quanta and $\mathbf{Q}$ are the nuclear coordinates of the normal modes. The vibrational branching ratios (VBRs) differ slightly from the FCFs due to the wavelength dependence of the spontaneous emission rate. For a Franck-Condon transition between two vibrational states $|v''_k\rangle$ and $|v'_k\rangle$, the VBR is defined as $\text{VBR} = \omega^3_{v'_k,v''_k} q_{v'_k,v''_k} / \left[\sum_{i,j}(\omega^3_{v'_i,v''_j} q_{v'_i,v''_j})\right]$, where $\omega_{v',v''}$ is the transition wavelength between $|v''\rangle \rightarrow |v'\rangle$ and the variables i, j index over the set of vibrational states that are coupled by radiative emission in the vibronic band.

Typically, $10 - 10^2$ photons are needed for realizing high fidelity optical state preparation, readout, and state control. Similar numbers of photons can also be utilized for radiative deflection[107,108], steering, and confinement[50,52] of a cryogenic molecular beam. For laser slowing and capture of a small polyatomic molecule, up to $10^4 - 10^5$ photons are typically needed. This threshold, however, can be decreased significantly via indirect slowing and cooling methods, such as Stark/Zeeman deceleration[109–113], optoelectric slowing and cooling schemes[114,115], as well as Zeeman-Sisyphus slowing[116–118], which can precede direct loading into a magnetic trap[119]. Magnetically assisted approaches to slowing and trapping may be especially well-suited for multi-electron OCCs due to the presence of high-spin ground and metastable electronic states, as further discussed in Sec. 5.

As we shall see, the *p*-block metals we consider make molecules which are bent. Unlike the highly symmetric species that have been previously laser-cooled, the molecules we consider are at most C_s symmetric and classified as asymmetric top molecules (ATM). ATMs, which possess three unequal moments of inertia ($I_A \neq I_B \neq I_C$), have electronic bands that can be categorized as *a*-type, *b*-type, or *c*-type, depending on the orientation of the transition dipole moment (TDM) relative to the molecule's three principal axes (*a*, *b*, *c*) (see Fig. 3 and Table 1). Each band has approximate angular momentum selection rules that can be leveraged to realize rotationally closed repump schemes with a manageable number of sidebands, as was shown in[26] for monovalent ATMs. This approach readily extends to multivalent ATMs, and a detailed discussion can be found in Appendix B of the electronic supplementary information (ESI).

Monovalent ATMs with optical cycling centers based on alkaline-earth metals have been previously considered[26], and suitable ligands were found to maintain optical cycling characteristics despite their lower symmetry. In the systems we consider, we find that using an ATM structure is in fact generally *necessary* for designing OCCs based on *p*-block metals, as linear analogs broadly appear to fail (see Appendix A(4) in the ESI).

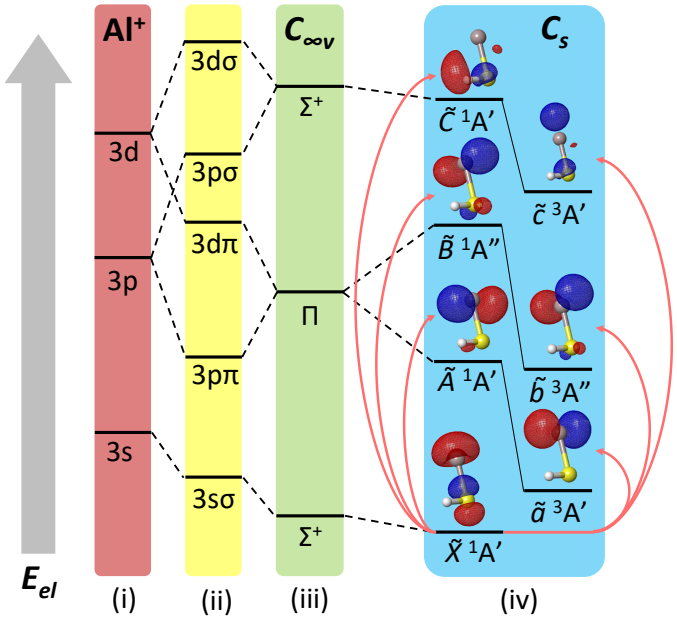

Fig. 2 Ligand field diagram for low-lying electronic states of AlSH, not to scale. States are arranged bottom-up by increasing electronic energy (E_{el}). On the farthest left are (i) Al^+ cation shells, which are then split by the ligand ($-SH^-$) field into (ii) molecule-frame projections of orbital angular momentum ($\Lambda = \sigma, \pi, \delta, ...$). These orbitals mix to yield the electronic manifolds in the (iii) $C_{\infty v}$ linear and (iv) C_s bent limits of the molecule. Above each excited manifold in the bent case are natural transition orbitals (isovalue = 0.05) from the ground state computed using EOM-EE-CCSD. See Appendix A(1) in the ESI for a complete list of molecular orbital (MO) correlation diagrams and natural transition orbitals for relevant species.

2 Computational Approach

We proceed by performing *ab initio* analyses of the electronic and rovibrational structure of several polyatomics of the *MXH* form. The molecular candidates that we consider have three distinct typologies, with singlet, doublet, or triplet spin multiplicities in the ground state. This organization generally corresponds to a group 13 (divalent), 14 (trivalent), or 15 (quadrivalent) optical cycling center, respectively, attached to a pseudohalogen.

The systems we consider possess ground states that at structural equilibrium are dominated by a single electronic configuration, making them ideally suited for analysis using coupled cluster methods[120]. Calculations of the ground states are performed using coupled cluster with singles and doubles (CCSD), and excited states are characterized using analogous equation-of-motion schemes (EOM-CCSD). EOM-CC approaches, which are rigorously size-extensive, allow for multiconfigurational descriptions of target states within a single-reference formalism[121] and have been previously validated[22,23,122–125] for predicting the properties of a broad range of laser-coolable diatomic and polyatomic molecules. In this work, the traditional EOM excitation

energies scheme (EOM-EE-CCSD)[126] is used to study molecules with ground state singlet and triplet configurations (e.g. AlSH and PSH) from a singlet reference wavefunction, while spin-flip (EOM-SF-CCSD)[127,128] is utilized for targeting states from a high-spin quartet reference (e.g. SiSH).

All electronic structure calculations are performed using the QChem 5.4 package[129], with wavefunction analyses conducted via the *libwfa* library[130]. Harmonic FCFs including Duschinsky rotation are computed using the *ezFCF* code[131]. Correlation-consistent sets of aug-cc-pVTZ(-PP) quality[132–134] are used for calculations of single point energies, geometries, frequencies, and transition intensities. For atoms heavier than period 3, core electrons are modeled using Stuttgart-type small core pseudopotentials (ECP10MDF, ECP28MDF, ECP60MDF)[135,136]. To infer periodic trends, we utilize atomic partial charges calculated from the intrinsic atomic orbitals (IAO) developed by Knizia[137], which are supplemented by Mulliken, natural population,[138,139], and electrostatic potential-based analyses[140–142] in Table S7 of the ESI.

Spin-orbit matrix elements are calculated perturbatively in the QChem code using the Breit-Pauli (BP) Hamiltonian[143–145], for which we utilize relativistically contracted all-electron atomic natural orbital (ANO-R0) sets[146] on the metal and metalloid cycling centers. These matrix elements, which are tabulated in Table S5, are used in combination with equilibrium EOM-CC energies (see Table S1-S3) to construct an effective Hamiltonian of the spin-orbit coupled states and obtain intersystem transition dipole moments. Prior studies[147] found that BP approaches – despite excluding non-perturbative relativistic effects – are able to capture dominant spin-orbit contributions, even in period 6 and 7 systems.

3 Vibronic Structure

3.1 Singlet Ground States: Group 13

The simplest multivalent case we consider is a singlet system that arises from bonding a group 13 (i.e. B, Al, Ga, In, Tl) center to a pseudohalogen ligand. Among diatomic molecules, AlF[86,87] and AlCl[88] have strongly electronegative bonds and highly diagonal cycling transitions. One might expect, as with the alkaline earth series of polyatomics, that replacing the halogen atom with electronegative pseudohalogens, such as hydroxide (-OH), cyanide (-CN), ethynyl (-CCH), or boron dioxide (-OBO) ligands, would yield similarly laser coolable molecules. This turns out to be not the case (see Appendix A(4) in the ESI). Instead, we find that strongly bent molecules containing ligands with less electronegative character, such as hydrosulfide (-SH), do possess suitable bonding and diagonal cycling transitions. Evidently, the unique orbital hybridization that enables laser cooling in AEL species does not universally translate to cycling centers from other columns of the periodic table.

A model system that we consider is the multivalent polyatomic alumininum monohydrosulfide (AlSH). In the ground state configuration¶ ($\tilde{X}^1A'$), the Al-S bond is partially ionic, with an IAO charge (Q_{IAO}) of $+0.36$ on the metal and -0.44 on the sulfur. This corresponds to the withdrawal of a single sp-hybridized valence electron from the Al atom, leaving an Al($3s\sigma$) lone pair polarized away from the bond. The S-H bond is almost orthogonal ($\sim 90.19°$) to the Al-S bond, forming a prolate asymmetric top with C_s symmetry. As we shall see, this bond angle is a very important feature. The optimized geometry has three normal modes, which approximately correspond to Al-S stretch (ν_1), Al-S-H bend (ν_2), and S-H stretch (ν_3), which are depicted in Fig. 3.

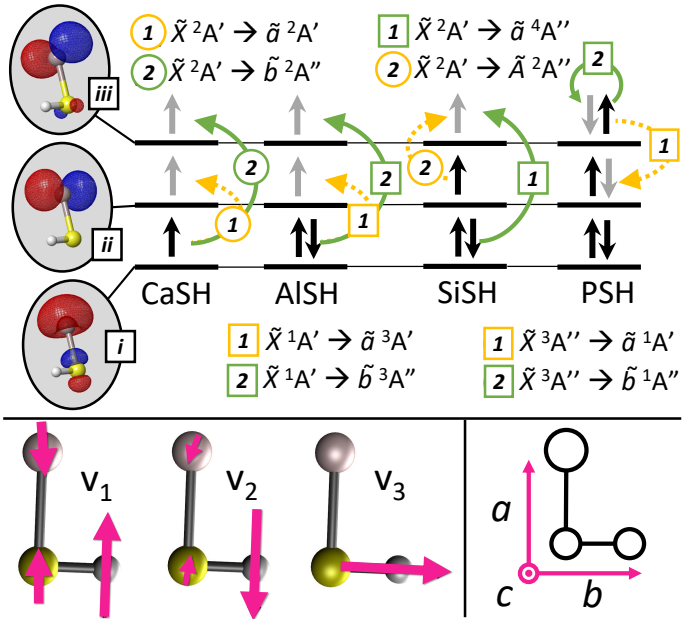

Fig. 3 Top: Electronic configuration for ground and low-lying excited states of group 2 (CaSH[26]), group 13 (AlSH), group 14 (SiSH), and group 15 (PSH) molecules. Depicted in the gray ovals on the left are frontier metal-centered MOs approximately corresponding to (i) $M^+(s\sigma)$, (ii) $M^+(p\bar{\pi})$, and (iii) $M^+(p\pi)$ atomic orbitals. Dashed yellow and solid green colored arrows depict (1) cycling and (2) intermediate decay channels, where circle and square labels indicate spin-allowed and spin-forbidden transitions. Black arrows in each MO denote electronic spins in the ground state configuration, while gray arrows denote electronic spins upon excitation. See Appendix A(1) in the ESI for complete MO and NTO schematics of low-lying electronic transitions. Bottom left: Vibrational modes roughly described as M-S stretch (ν_1), M-S-H bend (ν_2), and S-H stretch (ν_3) in a multivalent asymmetric top molecule. Bottom right: Rotational axis convention for asymmetric top molecules (see Appendix B in the ESI). By convention, the tuple $(\hat{a},\hat{b},\hat{c})$ maps to the unit vectors $(\hat{z},\hat{x},\hat{y})$ used to label atomic orbitals.

The lowest three triplet states are 2.3 to 4.2 eV above the ground state and roughly correspond to the excitation of a single Al-localized $3s\sigma$ electron to $3p\pi+3d\pi$ and $3p\sigma+3d\sigma$ orbitals. The $3s\sigma \rightarrow 3p\pi+3d\pi$ excitation is split by the off-axis SH ligand into an in-plane $\tilde{a}^3A'$ and out-of-plane $\tilde{b}^3A''$ state, while the $3s\sigma \rightarrow 3p\sigma+3d\sigma$ excitation corresponds to an on-axis $\tilde{c}^3A'$ state, as indicated by the ligand field diagram and natural transition or-

¶ In this work, we adhere to spectroscopic conventions for labeling electronic states. $\tilde{X}$ is always the ground state; excited states with the same spin multiplicity as $\tilde{X}$ are $\tilde{A},\tilde{B},\ldots$, whereas those with different spin multiplicity are $\tilde{a},\tilde{b},\ldots$, both ordered in increasing energy. The spin multiplicity is the superscript after the state name. A'' indicates the symmetry of the state, with A' (A'') indicating that the electronic wavefunction is in-plane (out-of-plane) as shown in Fig. 2.

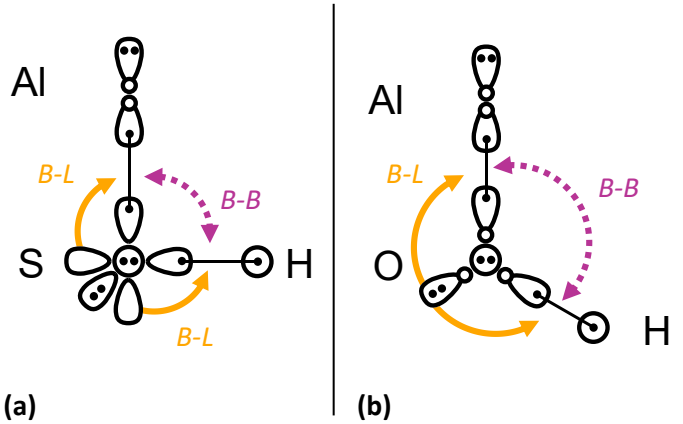

Fig. 4 Simplified valence bonding (VB) diagram for (a) AlSH and (b) AlOH. Arrows illustrate the two main repulsive effects involved in the geometry of the molecules: 1) the bond-bond repulsion between the aluminum-chalcogen and chalcogen-hydrogen bonds (purple dotted line, *B-B*) and 2) repulsion from the in-plane s lone pair on the chalcogen against the two bonds (yellow solid line, *B-L*). In the absence of strong bond-bond repulsion, the bonds lock into the near-90°geometry provided by the orthogonal p-orbitals on the coordinating atom. This is the case in (b) AlSH, where the $3p_z$ and $3p_x$ valence lobe orbitals (with + and − density components shown) on the coordinating sulfur bond to the H and to a sole $3sp$-hybridized electron on the Al. The doubly occupied sp orbital on the Al polarizes away from the Al-S bond, resulting in a 90°bond angle.The doubly occupied sp orbital on the Al polarizes away from the Al-S bond, resulting in a 90°bond angle. Remaining out-of-plane $3p_y$ (circle with two dots) and in-plane $3s$ (teardrop with two dots) lone pairs are depicted on the sulfur atom. Low-lying excited states are formed by excited one of the two electrons in the doubly occupied Al($3sp$) orbital to in-plane Al($3p_x$) and out-of-plane Al($3p_y$) orbitals. By contrast, in (b) AlOH, the short Al-O and O-H bonds lead to strong repulsion that opens the bond angle to >90°. This results in sp hybridization of the valence orbitals on the O atom, while the s lone pair builds in p-character. Additional details on this description can be found in Appendix A in the ESI(2), which includes generalized valence bond (GVB) natural orbitals and GVB diagrams for all three molecular classes.

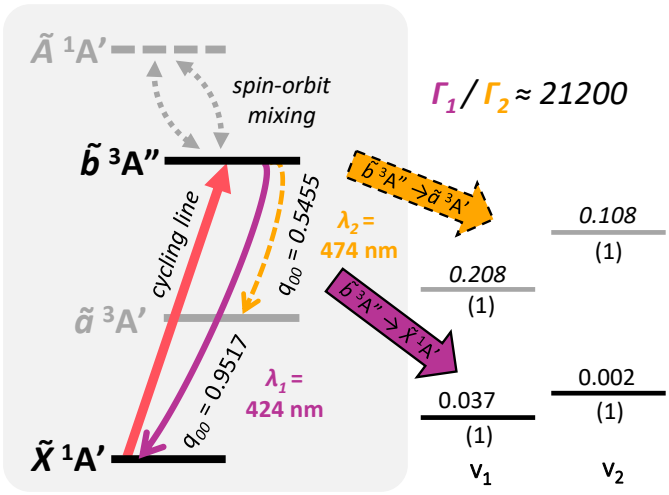

Fig. 5 Generic photon cycling scheme for group 13 molecules, using vibronic branching data from InSH. The main cycling transition (red solid arrow) is from $\tilde{X}^1A'$ to $\tilde{b}^3A''$. On the left, solid curved (purple) and dashed curved (yellow) lines denote vibration-free decays to vibrational channels in the $\tilde{X}^1A'$ and $\tilde{a}^3A'$ manifolds, respectively, after spontaneous emission from the $\tilde{b}^3A''$ upper cycling state. Pairs of gray dashed arrows depict the spin-orbit induced mixing between the first excited singlet state $\tilde{A}^1A'$ and the upper $\tilde{b}^3A''$ cycling state. Levels on the right hand side depict leading off-diagonal FCFs for decays to the $\tilde{a}^3A'$ and $\tilde{X}^1A'$ manifolds, with corresponding transition wavelengths denoted λ_2 and λ_1, respectively. Decimals above the levels denote the Franck-Condon factors (eq. 1) normalized relative to the respective electronic transition, while numbers underneath indicate the vibrational quanta in each mode (v_i). Due to spin-orbit effects from the In center, more than 99.995% of decays out of the $\tilde{b}^3A''$ state connect directly to the $\tilde{X}^1A'$ state, as indicated by the suppression factor (Γ_1/Γ_2) in the upper right hand corner (see Table 1). Note that level spacings are not drawn to scale.

bital (NTO) analysis in Fig. 2 (also see Fig. 6 and Appendix A(1) in the ESI). An analogous progression is obtained for the singlet states, which are all at ultraviolet energies. A summary of computed origins, rovibrational energies, and optimized geometries for both sets of states is listed in the ESI.

Out of these six lowest lying electronic states, which are computed using EOM-EE-CCSD, we find that the $\tilde{b}^3A'' \rightarrow \tilde{X}^1A'$ transition ($\Delta E \sim 2.74$ eV) provides extremely diagonal vibrational branching, with an FCF of $q_{0,0} > 0.997$ on the main vibrationless line. Dominant off-diagonal decays to $\tilde{X}$ are to the first ($q \sim 10^{-3}$) and second quanta ($q \sim 10^{-4}$) of the v_1 stretch mode. The $\tilde{b}^3A'' \rightarrow \tilde{X}^1A'$ vibrationless decay has one of the highest predicted FCFs among polyatomic systems that have been experimentally or theoretically characterized; however, as discussed later, losses from branching to intervening electronic states are non-negligible for this molecule.

This finding is in line with prior theoretical and spectroscopic investigations of the iso-electronic AlF[86] and AlCl molecules[88], which also found exceptionally high FCFs between the $X^1\Sigma^+$ state and $\{a^3\Pi,\ A^1\Pi\}$ manifolds. Benchmarks of our theoretical approach are in good agreement with observed geometries, energies, and lifetimes of AlF, AlOH, and AlSH (see ESI).

Meanwhile, the analogous $\tilde{b}^3A'' \rightarrow \tilde{X}^1A'$ transition in AlOH has very non-diagonal Franck Condon factors, with $< 30\%$ branching to the vibrationless ground state. There is an intuitive explanation for the diagonality of the $\tilde{b}^3A'' \rightarrow \tilde{X}^1A'$ transition in AlSH versus AlOH, based on qualitative arguments from valence bond (VB) theory[148] (see Fig. 4). The larger size and lower electronegativity of S versus O results in increased bond lengths and reduced repulsion between the Al-S and S-H bonding electrons. The residual repulsion from the in-plane S($3s$) lone pair then dominates, causing AlSH to lock into the near-90° bent configuration given by the (orthogonal) bonding p orbitals in S. We find that this geometry is stable when a valence electron around the Al atom is excited into an out-of-plane excited orbital, which is approximately decoupled from in-plane repulsive effects.

By contrast, the shorter bond lengths in AlOH (induced by the electronegativity of the oxygen atom) cause increased bond-bond repulsion that pushes the bond angle past 90°. This results in a bond angle that is highly sensitive to changes in orbital hybridization, and therefore highly non-diagonal Franck-Condon behavior. This VB picture is validated in Sec. 4 by high-level molecular orbital (MO)-based calculations, where we substitute even heavier atoms for S.

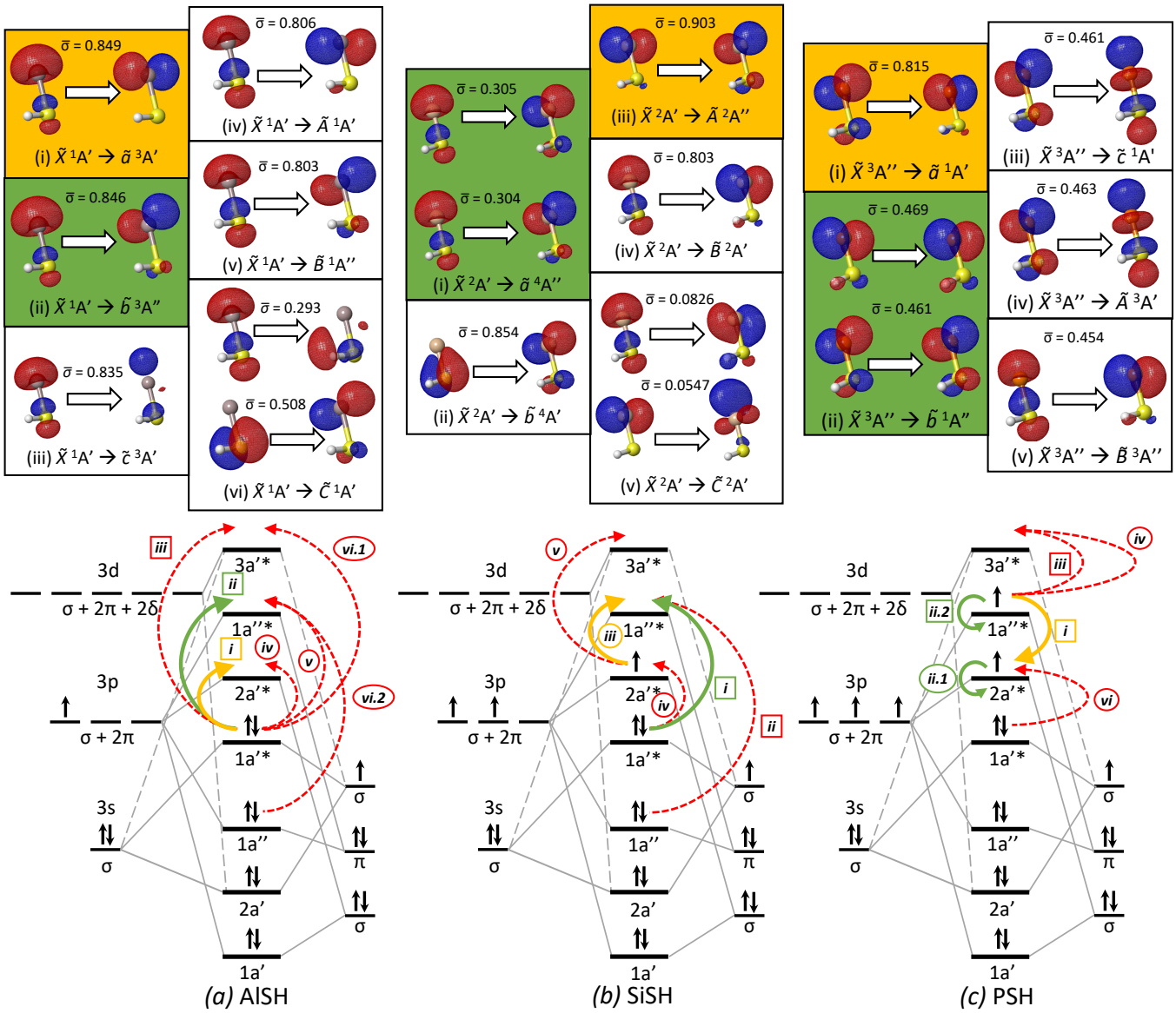

Fig. 6 Natural transition orbitals (isovalue = 0.05) for low-lying electronic transitions (top) and molecular orbital correlation diagrams (bottom) of three model multivalent species: (a) AlSH, (b) SiSH, and (c) PSH. Within each NTO panel are particle-hole pairs for the labeled transition, where $\bar{\sigma}$ denotes the relative NTO amplitude of each pair. Highlighted in green and yellow panels are the primary cycling and ground-to-intermediate state transitions, following the convention of Table 1. NTO calculations are performed using (a) EOM-EE-CCSD with a singlet ground state reference, (b) EOM-SF-CCSD with a quartet excited state reference, (c) and EOM-EE-CCSD with a singlet excited state reference. Below the NTO diagrams are MO correlation diagrams, which – for each of the three molecules – depict the ground state MO and spin configurations that are formed from the correlation of cycling center (left) and hydrosulfide ligand (right) orbitals. Each MO is labeled by its C_s symmetry character (A', A''), whereas the symmetry content of atomic and diatomic ligand orbital shells are labeled by $C_{\infty v}$ representations (σ, π, δ...), which are described in the text. Curved arrows correspond to hole-particle NTO transitions depicted in the upper panels, which are individually identified by roman numerals, with subdivisions for transitions with multiple significant NTO components. Transitions labels surrounded by circles and squares indicate spin-allowed and spin-forbidden transitions, respectively. The cycling and ground-to-intermediate state transitions are identified with green and yellow solid arrows, following the color convention in Fig. 3, while the remaining transitions are identified with dashed red arrows.

In contrast to the $\tilde{b}^3A'' \rightarrow \tilde{X}^1A'$ transition, the vibrationless transitions of AlSH from the other five excited manifolds to the ground state have either moderate (< 0.7) or poor (< 0.3) FCFs (see Table 1). The sub-optimal vibrational branching for the in-plane states $\{\tilde{a}^3A', \tilde{A}^1A'\}$ can be understood in terms of the repulsion between an in-plane Al($3p\bar{\pi}$) lobe with the S-H bond, thereby opening the excited state bond angle to $\sim 100^\circ$. This structural change drives vibrational branching to the bending mode (v_2) and Al-S stretch modes (v_1) during $\{\tilde{a}^3A', \tilde{A}^1A'\} \rightarrow \tilde{X}^1A'$ transitions. Conversely, UV excitations to the $\{\tilde{c}^3A', \tilde{C}^1A'\}$ states preserve the bond angle, but exhibit substantially longer ($> 28\%$) bond length and increased branching to the ground state v_1 mode.

Globally, we also observe that the triplet states have shorter bond lengths and more diagonal FCFs than the excited singlet states. The $\tilde{B}^1A'' \rightarrow \tilde{X}^1A'$ vibrationless decay, for instance, has an FCF of only ~ 0.2, with the primary v_1 loss attributable to an increased ($\sim 6\%$) Al-S bond length in the excited state. This effect can be rationalized as a consequence of spin-exchange effects between the frontier orbitals. In the low-lying A' and A'' excited states, a single valence electron from the doubly occupied metal $s\sigma$ antibonding orbital is promoted to the $p\bar{\pi}$ and $p\pi$ antibonding orbitals, respectively. As the singly occupied σ orbital is orthogonal to the singly occupied $p\bar{\pi}$ and $p\pi$ orbitals, spin-exchange interactions between the unpaired electrons in the triplet spin configurations contribute negatively[149] to the energy of the electronic configuration. By contrast, in the singlet spin configurations, spin-exchange interactions between the singly occupied, orthogonal orbitals contribute positively to the many-electron energy. Minimizing the electronic potential in singlet excited configurations therefore causes delocalization of the frontier π orbitals and lengthening of the M-S bond.

Interestingly, the states implicated in the $\tilde{b}^3A'' \rightarrow \tilde{X}^1A'$ diagonal transition for AlSH possess some antibonding character, as indicated by the presence of nodal planes across the Al-S bond in the hole-particle NTOs (see Fig. 3 and Fig. 6). Meanwhile, the particle orbital corresponding to the intermediate $\tilde{a}^3A'$ state possesses a more pure "atom-like" character, and has strongly shifted geometry relative to the $\tilde{X}^1A'$ ground state and therefore non-diagonal decays. This situation differs from the idealized picture established for monovalent MOR systems, where the diagonal decays typically originate from an "atom-like" excited state that is highly localized to the cycling center and does not participate in the bond[22]. The results here suggest that viable cycling transitions can exist in cases where the excited states are not strictly "atom-like," but have at least a similar degree of antibonding character relative to the ground state[||].

The relevant vibronic level schematic for group 13 molecules, including AlSH is shown in Fig. 5. In the case of AlSH, the cycling scheme is centered around a ~ 450 nm transition from $\tilde{X}^1A'$ to $\tilde{b}^3A''$. The upper $\tilde{b}^3A''$ state has $\sim 0.1\%$ and $\sim 0.02\%$ admixtures with the $\tilde{X}^1A'$ and $\tilde{A}^1A'$ manifolds due to spin-orbit coupling, resulting in an extremely narrow $2\pi \times 4.28$ Hz ($\mu \sim 2.81 \times 10^{-3}$ D) dipole-allowed transition from the ground state.[**] Electronic decays from $\tilde{b}^3A''$ to the intermediate $\tilde{a}^3A'$ states are calculated to have a transition dipole moment (μ) of $\sim 2.58 \times 10^{-2}$ D. Despite the larger transition moment of the intermediate decay, the intensity of this band is in fact suppressed by a ratio of 3.7:1 relative to the $\tilde{b}^3A'' \rightarrow \tilde{X}^1A'$ cycling transition (see Table 1). This comes as a consequence[150] of Fermi's Golden rule and the ω^3 scaling of radiative intensities for electric dipole transitions[151]; the smaller transition dipole moment of the $\tilde{b}^3A'' \rightarrow \tilde{X}^1A'$ decay is offset by its significantly shorter transition wavelength relative to the transition wavelength of the intermediate $\tilde{a}^3A' \rightarrow \tilde{X}^1A'$ decay.

The long lifetime of the excited state would result in very low scattering rates, making Doppler laser cooling not feasible for AlSH. However, since the transition dipole moment depends on the spin-orbit (SO) coupling, we can improve both the scattering rate and the $\tilde{b}^3A'' \rightarrow \tilde{a}^3A'$ branching by choosing heavier group 13 cycling centers with increased SO effects. This naturally also leads to an increased suppression factor for decays to the intervening $\tilde{a}^3A'$ electronic state, as the intensity of the dipole-allowed intermediate $\tilde{b}^3A'' \rightarrow \tilde{a}^3A'$ decays do not increase, and in fact, slightly decrease with the change to heavier metal centers. We find that substituting the Al cycling center with Ga and In atoms marginally decreases the vibrationless cycling line ($\tilde{b}^3A'' \rightarrow \tilde{X}^1A'$) FCF to 0.9804 and 0.9517, respectively, while significantly increasing the SO-induced linewidths to $2\pi \times 137$ Hz ($\mu \sim 1.32 \times 10^{-2}$ D) and $2\pi \times 2.91$ kHz ($\mu \sim 6.67 \times 10^{-2}$ D). The suppression factor into $\tilde{a}^3A'$ similarly increases to 86.5 : 1 GaSH and 21200 : 1 for InSH. Scattering of $> 10^4$ photons is therefore plausible before needing to repump out of the intermediate $\tilde{a}^3A'$ state for these heavier, isoelectronic species (see ESI for details). Note, however, that branching at the $\lesssim 10^{-4}$ level can be induced by vibronic effects[123,152], which are not considered here but warrant further study.

3.2 Doublet Ground States: Group 14

Next, we examine neutral polyatomic systems with group 14 (e.g. C, Si, Ge) optical cycling centers bonded to a hydrosulfide ligand (-SH). The molecules in this class have doublet ground states similar to monovalent alkaline earth-pseudohalogen systems, but a much larger valence space that includes ground state electron occupation in p-orbitals as well as s-orbitals localized to the optical cycling centers.

A model system is SiSH. In its ground state, the Si atom has two unpaired electrons in $3p_z$ and $3p_x$ orbitals, yielding a $(3s)^2(3p_z)(3p_x)$ valence configuration. Like AlSH, the ground state of SiSH consists of a bond between an unpaired Si($3p\sigma$) orbital, which has Si($3p_z$) character, and the unpaired SH σ-electron. The remaining in-plane $3p\bar{\pi}$ orbital Si($3p_x$) contains one unpaired electron and is the frontier orbital for a $^2A'$ electronic manifold. Meanwhile, the Si($3s$) lone pair mixes with the negative amplitude lobe of the $3p\sigma$ orbital to polarize against the new Si-S bond. (The positive amplitude component is oriented

[||] We thank an anonymous reviewer for making this subtle and insightful observation.

[**] This can be compared against transition widths for AEL-type monovalent OCCs, which are typically $\sim 2\pi \times 1 - 10$ MHz.

Table 1 Transition energies, wavelengths, vibrationless FCFs (q_{00}), linewidths, and band orientation (see Appendix B in the ESI) for cycling and decay transitions of MSH molecules. Data for intersystem lines assume intensity borrowing due to SO mixing.

	Cycling Transition ($\tilde{b}^3A'' \rightarrow \tilde{X}^1A'$)					Intermediate Decay ($\tilde{b}^3A'' \rightarrow \tilde{a}^3A'$)					
Species	ΔE (eV)	λ (nm)	q_{00}	Γ (s^{-1})	Band	ΔE (eV)	λ (nm)	q_{00}	Γ (s^{-1})	Band	Suppression
BSH	2.396	517	0.9600	$2\pi\times4.24$	*ab*-type	0.9350	1326	0.1708	$2\pi\times97.6$	*c*-type	0.0434
AlSH	2.744	451	0.9974	$2\pi\times4.28$	*ab*-type	0.4045	3065	0.5645	$2\pi\times1.16$	*c*-type	3.70
GaSH	3.113	398	0.9804	$2\pi\times137$	*ab*-type	0.4143	459	0.3658	$2\pi\times1.58$	*c*-type	86.5
InSH	2.921	424	0.9517	$2\pi\times2910$	*ab*-type	0.306	474	0.5455	$2\pi\times0.137$	*c*-type	21200
TlSH	3.330	372	0.5210	$2\pi\times681000$	*ab*-type	0.2297	400	0.2706	$2\pi\times0.00996$	*c*-type	6.83×10^7

(a) Group 13 molecules

	Cycling Transition ($\tilde{a}^4A'' \rightarrow \tilde{X}^2A'$)					Intermediate Decay ($\tilde{a}^4A'' \rightarrow \tilde{A}^2A''$)					
Species	ΔE (eV)	λ (nm)	q_{00}	Γ (s^{-1})	Band	ΔE (eV)	λ (nm)	q_{00}	Γ (s^{-1})	Band	Suppression
CSH	2.121	585	0.6667	$2\pi\times37.8$	*ab*-type	1.036	1143	0.3412	$2\pi\times0.0298$	*c*-type	1268
SiSH	2.654	467	0.7049	$2\pi\times192$	*ab*-type	2.090	593	0.7515	$2\pi\times0.219$	*c*-type	875
GeSH	2.845	436	0.2498	$2\pi\times770$	*ab*-type	2.319	535	0.5631	$2\pi\times2.37$	*c*-type	325

(b) Group 14 molecules

	Cycling Transition ($\tilde{b}^1A'' \rightarrow \tilde{X}^3A''$)					Intermediate Decay ($\tilde{b}^1A'' \rightarrow \tilde{a}^1A'$)					
Species	ΔE (eV)	λ (nm)	q_{00}	Γ (s^{-1})	Band	ΔE (eV)	λ (nm)	q_{00}	Γ (s^{-1})	Band	Suppression
PSH	0.8558	1449	0.9018	$2\pi\times8.86\times10^{-4}$	*c*-type	0.5307	2336	0.2986	$2\pi\times14.4$	*c*-type	6.13×10^{-5}
AsSH	0.8524	1455	0.9224	$2\pi\times0.900$	*c*-type	0.3773	3286	0.2690	$2\pi\times3.53$	*c*-type	0.255
SbSH	0.7897	1570	0.9572	$2\pi\times2.46$	*c*-type	0.1969	6297	0.5130	$2\pi\times0.214$	*c*-type	11.5
BiSH	0.7750	1600	0.9674	$2\pi\times6.19$	*c*-type	0.117	10566	0.3994	$2\pi\times0.0308$	*c*-type	200

(c) Group 15 molecules

towards the bond to maximize bonding overlap.) Quartet configurations can be obtained by exciting one of the Si($3s$) electrons into the out-of-plane Si($3p\pi$) orbital, which has Si($3p_y$) character, to obtain a $^4A''$ state (see Fig. 3, Fig. 6 and Appendix A(1) in the ESI). This configuration is analogous to high-spin states ($^4\Sigma^-$) that have been spectroscopically observed in diatomics such as CF[153], SiF[154,155], and GeF[156].

Calculations for group 14 molecules are performed via EOM-SF-CCSD, using this high-spin quartet $^4A''(m_s = 3/2)$ reference to target low-spin $m_s = 1/2$ states. Spin-contamination in both the high-spin reference and low-spin targets is not observed to be significant, and all state descriptions are approximately good eigenstates of $\hat{S}^2$ (see Table S8 in the ESI).

The ground state molecular geometry of SiSH is bent, with a bond angle of $\sim 100^\circ$. In analogy to earlier arguments, the larger bond angle can be attributed to repulsion between the S-H bond and the in-plane Si($p\bar{\pi}$) orbital. The Si-S bond is polar, with an IAO charge of $Q_{\mathrm{IAO}} = +0.17$ on the cycling center and $Q_{\mathrm{IAO}} = -0.24$ on S. Immediately above the ground state is a low-lying out-of-plane $\tilde{A}^2A''$ state (0.56 eV) and in-plane $\tilde{B}^2A'$ state (3.79 eV), which corresponds to excitations from the in-plane Si($3p\bar{\pi}$) to the out-of-plane Si($3p\pi$) and Si($3p\sigma$) orbitals, respectively. A high-spin $\tilde{a}^4A''$ state (2.65 eV) with occupation in an out-of-plane Si($3p\pi$) orbital is predicted between the two doublet excited states. Above all three states is the $\tilde{C}^2A'$ manifold (3.95 eV), which has occupation in Si($3d\sigma$).

The optimal cycling transition in this system is from the $\tilde{X}^2A'$ to the $\tilde{a}^4A''$ state. Between the $\tilde{a}^4A''$ and $\tilde{X}^2A'$ state is the low-lying intermediate $\tilde{A}^2A''$ state, which has non-diagonal decays to the ground state from the $\tilde{a}^4A''$ state. For the $\tilde{a}^4A'' \rightarrow \tilde{X}^2A'$ cycling transition, the vibrationless FCF is $q_{0,0} \sim 0.7049$, while the leading off-diagonal decay to the first quanta of the Si-S stretch mode (v_1) has an FCF of $q \sim 0.2081$. Subleading off-diagonal losses at the percent-level include decays to the first quanta of the v_2 bending mode ($q \sim 5.04\times10^{-2}$) and second quanta of the v_1 Si-S stretch mode ($q \sim 1.92\times10^{-2}$). Despite a lower vibrationless FCF than the group 13 and 15 systems considered earlier, the sum of the leading two FCFs for the SiSH $\tilde{a}^4A'' \rightarrow \tilde{X}^2A'$ transition exceeds 90% and the sum of the leading four FCFs exceeds 98%, which is comparable to the leading FCFs of the most diagonal polyatomic systems.

Intersystem transitions to the $\tilde{a}^4A''$ state are allowed via a combination of direct spin-orbit mixing with the X^2A' state and intensity borrowing from spin-allowed transitions to higher doublet states, resulting in kHz-scale scattering rates. Branching to the intermediate $\tilde{A}^2A''$ state is suppressed due to disfavored spin-orbit couplings by a factor of ~ 900 (see Table 1). Substituting the Si center for a Ge atom increases the scattering rate and suppression factor by a factor of ~ 3 at the cost of a lower vibrationless FCF. We further find that substituent cycling centers heavier than Ge (i.e. Sn and Pb) do not provide stable geometries for photon cycling between the $\tilde{a}^4A''$ and X^2A' states.

3.3 Triplet Ground States: Group 15

In this section, we consider group 15 (P, As, Sb, Bi) centers bonded to a hydrosulfide ligand (-SH) and find that this approach works well, despite possessing significantly different electronic configurations from the original group 13 prototype. Molecules with group 15 centers have ground triplet configurations, which provide for a unique set of properties to combine with optical cycling and polyatomic structure, including large magnetic moments and hyperfine states with widely tunable spin couplings in the ground electronic state.

We proceed with an analysis of the electronic structure of these

systems, which is conducted using EOM-EE-CCSD with a singlet reference. A prototypical case is PSH. Unlike the Al atom, which only has a single unpaired $3p\sigma$ electron in its ground state, the P atom has three singly occupied p-orbitals, corresponding to a $(3s)^2(3p_x)(3p_y)(3p_z)$ high-spin valence configuration. The unpaired P($3p\sigma$) orbital, which has P($3p_z$) character, pairs to an unpaired σ-orbital on the SH ligand, forming a polar covalent bond between the P ($Q_{IAO} = -0.00144$) and S ($Q_{IAO} = -0.0756$) atoms. The residual unpaired P($3p\bar{\pi}$) and P($3p\pi$) electrons, which have P(p_x) and P(p_y) character, form a $^3A''$ state. As before, the P($3s$) lone pair electrons polarize against the P-S bond by mixing with the negative amplitude lobe of the P($3p\sigma$) orbital. Singlet configurations of PSH correspond to the singlet pairing of the singly occupied P($3p\bar{\pi}$) and P($3p\pi$) orbitals ($^1A''$) plus the two states where either P($3p\bar{\pi}$) or P($3p\pi$) are doubly occupied (see Fig. 3 and Appendix A(1) in the ESI).

Due to nodal planes in the residual non-bonding P($3p\pi$) and P($3p\bar{\pi}$) orbitals, spin-exchange interactions favor a triplet over a singlet configuration in the ground state. The ground state of PSH therefore has the term $\tilde{X}^3A''$. In this state, PSH has a bond angle of 96°, slightly larger than that of AlSH. The lowest singlet states correspond to excitations from the out-of-plane P($3p\pi$) orbital to the in-plane P($3p\bar{\pi}$) orbital ($\tilde{a}^1A'$), the out-of-plane P($3p\pi$) ($\tilde{b}^1A''$), and the on-axis P($3d\sigma$) orbital ($\tilde{c}^1A'$). These singlet states have origins at 0.325 eV, 0.856 eV, and 3.962 eV, respectively. Triplet progressions to the in-plane and out-of-plane P($p\pi$) orbitals correspond to the $\tilde{A}^3A'$ (3.468 eV) and $\tilde{B}^3A''$ (3.740 eV) states.

Similar to our findings in the last section, we find that the $\tilde{X}^3A'' \rightarrow \tilde{b}^1A''$ transition provides the most diagonal vibrationless FCF and is therefore well-suited as a cycling transition. The main vibrationless decay has an FCF of $q_{0,0} \sim 0.9018$, with dominant decays to the first ($q \sim 0.0907$) and second ($q \sim 2.506 \times 10^{-3}$) quanta of the P-S stretch mode (v_1), the first ($q \sim 3.852 \times 10^{-3}$) quanta of the bending mode (v_2), and a $q \sim 6.621 \times 10^{-4}$ decay to a stretch-bend ($v_1 = 1, v_2 = 1$) combination state. Decays from and to in-plane states (such as the intermediate $\tilde{a}^1A'$ state) yield less diagonal FCFs, due to analogous bonding principles discussed in the previous section.

For group 15 systems, the spin-orbit interaction on the cycling center preferentially couples $\tilde{b}^1A''$ to in-plane triplet states over out-of-plane triplet states as a consequence of spatial selection rules (see Sec.4(B)). As the ground state is out-of-plane for this class of molecules, the intensity borrowing for the $\tilde{X}^3A'' \rightarrow \tilde{b}^1A''$ cycling transition is weaker than in group 13 systems, resulting in significantly narrower cycling transitions (see Table 1(b) and Sec. 4(A)). Conversely, the intermediate $\tilde{b}^1A'' \rightarrow \tilde{a}^1A'$ decay gains intensity through symmetry-favored spin-orbit couplings between the $\tilde{a}^1A'$ and $\tilde{X}^3A''$ state. As a consequence, suppression factors in group 15 systems are systematically reduced relative to their group 13 analogs.

As with group 13 molecules though, substitution of heavier cycling centers leads to broader cycling transitions and more heavily suppressed decays to the intermediate $\tilde{a}^1A'$ state. We also find that the vibrationless FCF on the cycling line is highly diagonal ($q_{0,0} > 90\%$) for all group 15 species and improves with heavier OCC substituents.

4 Design principles

4.1 Linker atom and bond polarity

The design of molecular OCCs requires cycling degrees of freedom to be decoupled from rovibrational modes of the molecule; that is – the geometry of the molecule should not change upon excitation in the optical cycling scheme. Linker atoms have a significant influence on cycling characteristics in polyatomic systems, both by controlling the nature of the OCC-ligand bond, as well as spatially decoupling the rovibrational modes of the ligand from metal-centered cycling. Among conventional AEL-pseudohalogen systems, the MO*R* motif, which utilizes an oxygen atom to link cycling centers (*M*) to a functional group (*R*), has seen enormous success in identifying and engineering laser-coolable systems [18,19,22,23,25,27–29,49–53,157–161]. Other linker paradigms (e.g. S, N, C) have also been explored for monovalent molecules [18,20,21], particularly systems of reduced symmetry [26].

In our analysis, we have considered the effects of a variety of chalcogens (X=O, S, Se, Te, Po) as coordinating atoms for optically active polyatomics. The lightest of all the possible choices is oxygen, which – as mentioned earlier – is widely used as a linker atom in monovalent, laser coolable polyatomics. Bonds that are coordinated to the p-electrons of oxygen naively adopt a perfect 90° angle, due to the orthogonality of the atomic orbitals. This geometry, however, is further altered by electrostatic mechanisms. In the case of oxygen, the electronegative character of the atom produces a highly polar metal-ligand bond, which has two effects on the structure of these molecules. First, the ionicity of the bond causes coulombic and bond-bond repulsion effects (which are optimal in the linear case) [162–164] to overcome repulsion from the in-plane oxygen lone pair (which prefers an acute structure) [165], resulting in a linear or highly symmetric nonlinear molecular geometry. Second, the highly polar metal-ligand bond polarizes the unpaired cycling electron away from the bond, decoupling it from the rest of the molecule. Indeed, it has been widely suggested in the cold molecule community that the existence of a highly polar bond between the OCC and ligand may be an important condition for diagonal FCFs and laser coolability [9,18,19,22–24,27–29].

By contrast, multivalent species with p-block OCCs and an oxygen linker (i.e. AlOH) have nonlinear geometries. This is due to the decreased polarity of the p-block metal-oxygen bond, which competes with the orthogonal configuration of the oxygen atomic orbitals involved in the bond. We find that the highly electronegative nature of the oxygen atom disrupts the vibrationless FCFs of p-block systems by causing large bond angle deflection upon excitation. This can be attributed to short metal-oxygen and oxygen-pseudohalogen bond lengths in the ground state, which induces bond-bond repulsion that works against the repulsive effects of the in-plane oxygen $3s$ lone pair and the T-shaped preference of the oxygen bonding orbitals. The result is an intermediate bond angle[††] that is much larger than 90°, but smaller than 180°(see

†† The rotational [166] and photoionization [167] spectra of AlOH suggests that the molecule

Fig. 4(a)). As seen in our calculations (see Fig. 7), the balancing of these competing effects creates a bond angle that is very sensitive to changes in the metal-oxygen bond hybridization, with $\Delta\theta > 30^\circ$ shifts in the bond angle upon excitation from the ground state.

Using an atom larger than oxygen decreases the metal-ligand bond polarity, but also decreases bond repulsion. This produces a ground state bond angle that is close to 90° and also more stable upon excitation (see Fig. 4(b)). We find that sulfur and selenium are ideal linker atoms that satisfy this requirement. This is consistent with MO trends‡‡ in the chalcogen hydrides (XH), which exhibit an increasing barrier to *sp* hybridization with chalcogen atomic number (as correlated with the $^4\Sigma - ^2\Pi$ bandgap), and therefore an increased propensity for a highly bent geometry coordinated to the *p*-orbitals of the chalcogen. Linker atoms heavier than period 4 (i.e. tellurium and polonium) also produce molecules with acceptable FCFs, although the larger spatial extent of the heavy chalcogen lone pair results in an acute ground state bond angle. Fig. 7 displays a chart of ground and excited state bond angles and metal-ligand IAO partial charge differences against choice of linker atom.

Superficially, these results suggest a new, if counter-intuitive, heuristic: in bent, multivalent species, linker substitutions that create *less polar* bonds may in fact result in *more diagonal* FCFs. A more complete explanation is that laser coolable polyatomics with stable bond angles are likely to be found at opposite ends of the metal-ligand ionicity spectrum, where the molecule is either linear (i.e. CaOH) or T-shaped (i.e. CaSH), but not in the intermediate regime (i.e. AlOH), where there are multiple competing repulsive effects.

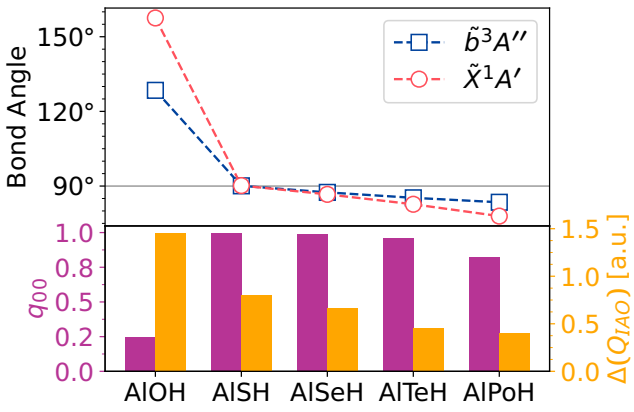

Fig. 7 Effects of chalcogen substituents on Franck-Condon factors, molecular geometries, and bond polarity. Line plot depicts bond angles for the cycling states $\tilde{X}^1A'$ and $\tilde{b}^3A''$ of five different AlXH molecular species with different chalcogen linker atoms [X=O, S, Se, Te, and Po]. Pairs of bar plots in the lower half of the panel indicate FCFs (left, purple) and IAO partial charge difference (Q_{IAO}, right, yellow) between the cycling center and linker atoms. A thin horizontal gray line on the upper plot denotes 90° bond angle.

4.2 Spin-orbit coupling and mass tuning

The spin and spatial mechanisms that provide for highly diagonal cycling schemes in the multivalent OCCs considered in this work also lead to transitions that are partially forbidden by both spin and orbital selection rules. This makes the spontaneous emission rates, and therefore the performance of cycling schemes, strongly dependent on the strength of spin-orbit effects induced by the cycling center.

As discussed earlier, intersystem transitions, including the primary cycling lines for all three classes of multivalent polyatomics discussed in this manuscript, gain intensity from both dipole-allowed transitions and the ground state dipole moment via spin-orbit coupling. In operator form, the molecular spin-orbit term ($H_{so} \propto \mathbf{L}\cdot\mathbf{S}$) can be expressed as [171]:

$$H_{so} = A_{so}[\mathbf{L}_z\mathbf{S}_z + (\mathbf{L}_+\mathbf{S}_- + \mathbf{L}_-\mathbf{S}_+)/2]. \quad (2)$$

For valence electrons centered around a single atom, the molecular spin-orbit constant A_{so} roughly scales as Z^2, thus favoring multivalent species with heavier OCCs, as seen earlier. The $\mathbf{L}_z$ and $\mathbf{S}_z$ operators act diagonally on molecule-frame projections of orbital $|\Lambda\rangle$ and spin $|\Sigma\rangle$ angular momentum, respectively, while cross-terms in the remaining half of eq. 2 mix states with $\Delta\Lambda = \pm 1$ and $\Delta\Sigma = \mp 1$. MOs spaced apart by one quanta of orbital angular momentum are therefore maximally mixed by spin-orbit coupling. This leads to a geometric selection rule (colloquially referred to as the "90 degree" or El-Sayed's rule) that orbitals with orthogonal spatial components have the largest amount of spin-orbit mixing and intersystem crossing [172–175].

Unlike in linear and highly symmetric molecules, Λ and Σ are not good quantum numbers in ATMs due to the breakdown in the intermolecular axis of symmetry. Nonetheless, geometric selection rules for spin-orbit mixing still apply to component atomic orbitals, leading to rigorous mixing rules for MOs by their in-plane (A') and out-of-plane (A'') character. Indeed, we observe in our candidate systems that strong SOC arises between electronic states of orthogonal symmetry, and weak or zero SOC manifests between electronic states of the same symmetry.

This has implications for expected scattering rates of intersystem cycling transitions and suppression factors in multivalent species, as the largest SOC – and therefore strongest intensity borrowing – is expected when there are nearby orthogonal-symmetry electronic states to which the spin-forbidden excited state can couple. Furthermore, the most intense dipole-allowed transitions occur between states of the same symmetry, which accordingly lead to more favorable intensities for nearby spin-forbidden lines. We can therefore deduce a general heuristic that more intense intersystem cycling transitions can be found in heavy multivalent species with level structure that supports: 1) an upper spin-forbidden electronic state with orthogonal symmetry to the ground state and 2) a closely lying dipole-allowed manifold with the same symmetry as the ground electronic state.

This is the case for singlet group 13 and doublet group 14 sys-

is quasi-linear, with large amplitude bending motion. This is consistent with theoretical studies that indicate a flat ground state bending potential [168] which supports a true bent equilibrium at ∼160° [169] and a low-lying quasi-linear transition state [170].

‡‡ We thank the anonymous reviewers for suggesting this interpretation.

tems considered in this manuscript, where an out-of-plane (A'') upper state couples strongly with an in-plane (A') ground state and the dipole-allowed progression to a nearby in-plane (A') excited state, resulting in moderate to high cycling scattering rates. Conversely, both cycling scattering rates and suppression factors for triplet group 15 systems are reduced due to the presence of a $^3A''$ ground state with the same symmetry as the $^1A''$ upper cycling state as well as symmetry-favored intensity borrowing between the $^3A''$ ground state and orthogonal $^1A'$ excited states that can interrupt the cycling scheme.

5 Outlook

5.1 Production

Cryogenic buffer-gas cooling[176] is a standard approach for producing large amounts ($> 10^{10}$ per pulse) of cold, slow, gas-phase molecules. This technique enables rapid thermalization and relaxation of "hot" reaction products through collisions with He (or other inert) buffer gas in a cryogenically cooled cell. A small aperture allows extraction of cold molecules via hydrodynamic entrainment in the buffer gas. A wide variety of organic and metallic molecules have been cooled using this technique, which is an important tool in molecular laser cooling and precision measurement.

While many of our candidate molecules have yet to be experimentally produced and observed, cryogenically compatible pathways have been established for synthesizing numerous gas-phase metallic analogs at high densities. Typical approaches to gas-phase synthesis involve Nd:YAG laser ablation of a solid metal target, followed by the introduction of a gas or liquid-phase precursor to produce the desired target species. For instance, thiol compounds with alkali[177–179], alkaline earth[180–183], (post-)transition metal centers[184,185] – including aluminum[186] – (MSH) are routinely produced in the gas phase via evaporation or ablation of solid metals in the presence of H_2S gas. Synthesis of larger polyatomics could potentially involve using liquid or gas-phase methanethiol, ($HSCH_3$), ethanethiol (HSC_2H_5), pentadienyl (C_5H_5), or benzene (C_6H_6) precursors, in a similar manner to the production of oxygen-containing polyatomics with capillary-introduced alcohol reactants (i.e. CH_3OH, C_2H_6O)[28,29,152,159,187–191]. Cryogenic yields can be further enhanced via state-selective excitation of reactants, as was demonstrated in the buffer-gas synthesis of YbOH molecules[192,193].

5.2 Applications

Multivalent optical cycling centers offer new avenues for quantum control, state preparation, and measurement with cold molecules. As mentioned in the introduction, multi-electron degrees of freedom have been leveraged extensively in cold atom experiments utilizing alkaline earth and transition metal species. Here, we have demonstrated a pathway to combining multivalent optical cycling centers with the range of features present in polyatomic molecular structure.

5.2.1 Trapping and Control

As in multi-electron atoms, the presence of two or more optically active electrons in molecular OCCs gives rise to tunable spin degrees of freedom. Higher-than-single valence OCCs, in particular, can support states with a wide range of electronic spins $S > 1/2$ and projections $m_s = \{-S, +S\}$. For instance, multivalent molecules with states possessing integer spins $S = \{0, 1\}$, such as those with group 13 and 15 OCCs, generically contain zero magnetic projection ($m_s = 0$) states, where the sensitivities to external magnetic fields and couplings to internal hyperfine structure (e.g. $\mathbf{I} \cdot \mathbf{S}$) are suppressed, as well as high spin projection states $m_s = 1$ where magnetic couplings are maximal.

Naturally, multivalent OCCs also possess metastable electronic states with flipped spin multiplicity from the ground state. These states, which were discussed extensively in earlier sections in the context of photon cycling, could also serve as shelving states for state preparation and detection as well as long-lived storage or measurement states for quantum information and sensing applications. Crossings between the scalar polarizabilities of ground and spin-forbidden excited states, meanwhile, give rise to perturbation-free "magic" dipole trapping wavelengths relative to transitions between the two states[59–61].

Due to their high electron-spin states, multivalent molecules are compelling candidates for magnetically assisted slowing and trapping. One demonstrated approach is Zeeman-Sisyphus deceleration[116–118] of a cryogenic beam, which can be followed by direct loading into a deep magnetic[119,194,195] or optical trap. This overcomes the limitation of direct Doppler slowing or trapping on narrowline intersystem transitions, while preserving photon budgets for high-fidelity state preparation and readout, or laser cooling of magnetically trapped molecules to ultralow Doppler temperatures.

Alternatively, large radiative forces can be exerted directly on the molecules by using coherent techniques to bypass spontaneous emission. The use of multiphoton or stimulated optical techniques – such as CW polychromatic forces[108,196–200] or ultrafast chirped π-pulses[201,202] – could extend experimental flexibility by increasing effective scattering rates for narrow cycling transitions identified in this work. Strong field or light-dressing schemes, in analogy to optical quench techniques used to cool on narrowline transitions of light AEL atoms (e.g. Ca[203], Mg[204]), may also be useful for decreasing effective lifetimes of excited cycling states in multivalent polyatomic species, potentially increasing scattering rates at the cost of mixing in transitions with less diagonal VBRs.

5.2.2 Quantum simulation and information

In addition to offering unique control properties, the internal structure generated by higher electronic valences in polyatomic molecules could offer new avenues for encoding quantum information, particularly in electron and nuclear spins[205,206], but also in low-lying rotational degrees of freedom. Structural asymmetry, as seen in bent MSH molecules, may also confer particular advantages for implementing error correction protocols[4]. Tunable spin couplings within multivalent molecules could also have utility in many-body quantum simulation. This can be illustrated via

analogy with the structure of AEL atoms, which have been leveraged to simulate high-dimensional SU(N) Hamiltonians through nuclear spin-independence [72–77] as well as study multi-orbital physics via orbital Feshbach resonances [207,208] and spin-orbital effects [208–213]. Incorporating tunable multi-electron degrees of freedom with the unique benefits of polyatomic molecular structure [8,102] (e.g. high polarizability, metastable co-magnetometers) could point to new directions in studies of strongly correlated quantum systems [103,104,214].

5.2.3 Precision measurement

The multivalent OCC paradigms developed in this work could also be useful for future precision searches of fundamental symmetry violations and beyond Standard Model physics in optically controllable heavy molecules [9,215,216]. Due to simple periodic prevalence, many isotopes that are sensitive to new physics possess complex transition and post-transition metal electronic valences, which pose obstacles to the engineering of cycling behavior [105]. Of particular relevance to this work are the p-block elements Tl and Pb, which possess high sensitivity to T- and P-violation via effects such as the electron EDM and nuclear Schiff moments [105,217–220]. The p-block, in particular, contains several nuclei which are (or nearly are) doubly magic. This condition makes many-body calculations of nuclear parity-violating effects, such as anapole moments, significantly more tractable and provides an important venue for interpreting measurements of nuclear properties [221–223]. Inserting these heavy centers into polyatomic molecules would yield intrinsically sensitive internal states [157,224] that simultaneously possess parity doublets and high polarizability useful for experimental measurements [8,102].

5.2.4 Extensions to complex molecules

In addition to exploring different choices of metal centers, ligand design may offer new internal structures and features. A particularly promising avenue is ligand functionalization of multivalent OCCs via an M$S$$R$-type motif where R is a complex or chiral functional group. Prior experimental and theoretical studies with monovalent OCCs have found that AEM-pseudohalogen systems of the M$O$$R$, M$S$$R$, and M$R$-type possess properties favorable for laser cooling [18,22,26,159–161,191], including cases where R is a complex organic ligand [19,27,158,225] up to as large as 60 atoms in size (i.e. fullerene) [25]. Preliminary results suggest that large, multivalent MSR-type molecules also exhibit structural features conducive to photon cycling, including OCC-localized frontier orbitals with visible-wavelength energy spacings. Combining multi-electron OCC structure with complex electronic ligand degrees of freedom, such as via hypermetallic functionalization [20,21], or tuning Franck-Condon factors via ligand substitution [22,27–29] offers yet more unexplored design space.

6 Conclusions

In this work, we have developed new design principles for engineering optical cycling into polyatomic molecules with multi-electron degrees of freedom, for which traditional design approaches fail. Using these paradigms, we have found several prototypical and candidate multivalent systems (MXH) that demonstrate properties favorable for optical cycling. Theoretical characterization indicates that these systems possess quasi-closed photon cycling schemes, exhibiting highly diagonal Franck-Condon factors and visible or near-visible transition wavelengths, with scattering rates dependent on spin-orbit mixing. These systems are prime candidates for further spectroscopic and computational investigations, which will be needed to devise tailored photon cycling and state control schemes for each molecule.

Through our analysis of multivalent OCCs, we have also elucidated the unique bonding and electrostatic mechanisms that enable highly diagonal cycling transitions in candidate systems. We have furthermore identified structural motifs that allow us to scale multivalent features to more complex polyatomic systems, including chiral and large organic functional groups. Our results provide new directions towards designing optical cycling enters in polyatomic molecules with complex electronic structure.

Author Contributions

P. Y. and N. R. H. conceptualized the project. P. Y. and A. L. conducted the calculations and analysis. W. A. G. advised on methodology and interpretation of the results. P. Y. wrote the manuscript and all authors contributed to the final text.

Conflicts of interest

There are no conflicts to declare.

Acknowledgements

We thank Benjamin Augenbraun, Lan Cheng, Arian Jadbabaie, Anna Krylov, Nick Pilgram, and Paweł Wójcik for insightful discussions and input. We also thank the anonymous referees for thoughtful feedback, which greatly improved the presentation of our results. P. Y. acknowledges support from the Eddleman Graduate Fellowship through the Institute for Quantum Information and Matter (IQIM), the Gordon and Betty Moore Foundation (7947), and the Alfred P. Sloan Foundation (G-2019-12502). A. L. acknowledges support from the C. S. Shastry Prize and the Caltech Associates SURF Fellowship. W. A. G. was supported by the Ferkel Chair. N. R. H. acknowledges support from the U.S. Department of Energy (DOE), Office of Science, Basic Energy Sciences (BES), under Award No. DE-SC0019245. The computations presented here were conducted in the Resnick High Performance Computing Center, a facility supported by the Resnick Sustainability Institute at the California Institute of Technology.

Notes and references

1 D. DeMille, *Physical Review Letters*, 2002, **88**, 067901.
2 K. K. Ni, T. Rosenband and D. D. Grimes, *Chemical Science*, 2018, **9**, 6830–6838.
3 P. Yu, L. W. Cheuk, I. Kozyryev and J. M. Doyle, *New Journal of Physics*, 2019, **21**, 093049.
4 V. V. Albert, J. P. Covey and J. Preskill, *Physical Review X*, 2020, **10**, 031050.
5 S. A. Moses, J. P. Covey, M. T. Miecnikowski, D. S. Jin and J. Ye, *Nature Physics*, 2017, **13**, 13–20.

6 J. L. Bohn, A. M. Rey and J. Ye, *Science*, 2017, **357**, 1002–1010.

7 J. A. Blackmore, L. Caldwell, P. D. Gregory, E. M. Bridge, R. Sawant, J. Aldegunde, J. Mur-Petit, D. Jaksch, J. M. Hutson, B. E. Sauer, M. R. Tarbutt and S. L. Cornish, *Quantum Science and Technology*, 2018, **4**, 014010.

8 I. Kozyryev and N. R. Hutzler, *Physical Review Letters*, 2017, **119**, 133002.

9 N. R. Hutzler, *Quantum Science and Technology*, 2020, **5**, 044011.

10 N. Balakrishnan, *J. Chem. Phys.*, 2016, **145**, 150901.

11 P. Puri, M. Mills, C. Schneider, I. Simbotin, J. A. Montgomery, R. Côté, A. G. Suits and E. R. Hudson, *Science*, 2017, **357**, 1370–1375.

12 M.-G. Hu, Y. Liu, D. D. Grimes, Y.-W. Lin, A. H. Gheorghe, R. Vexiau, N. Bouloufa-Maafa, O. Dulieu, T. Rosenband and K.-K. Ni, *Science*, 2019, **366**, 1111–1115.

13 L. W. Cheuk, L. Anderegg, B. L. Augenbraun, Y. Bao, S. Burchesky, W. Ketterle and J. M. Doyle, *Physical Review Letters*, 2018, **121**, 083201.

14 S. Ding, Y. Wu, I. A. Finneran, J. J. Burau and J. Ye, *Physical Review X*, 2020, **10**, 021049.

15 L. Anderegg, L. W. Cheuk, Y. Bao, S. Burchesky, W. Ketterle, K.-K. Ni and J. M. Doyle, *Science*, 2019, **365**, 1156–1158.

16 L. W. Cheuk, L. Anderegg, Y. Bao, S. Burchesky, S. S. Yu, W. Ketterle, K.-K. Ni and J. M. Doyle, *Physical Review Letters*, 2020, **125**, 043401.

17 L. Caldwell, H. J. Williams, N. J. Fitch, J. Aldegunde, J. M. Hutson, B. E. Sauer and M. R. Tarbutt, *Physical Review Letters*, 2020, **124**, 063001.

18 T. A. Isaev and R. Berger, *Physical Review Letters*, 2016, **116**, 063006.

19 I. Kozyryev, L. Baum, K. Matsuda and J. M. Doyle, *ChemPhysChem*, 2016, **17**, 3641–3648.

20 M. J. O'Rourke and N. R. Hutzler, *Physical Review A*, 2019, **100**, 022502.

21 M. V. Ivanov, S. Gulania and A. I. Krylov, *The Journal of Physical Chemistry Letters*, 2020, 1297–1304.

22 M. V. Ivanov, F. H. Bangerter and A. I. Krylov, *Physical Chemistry Chemical Physics*, 2019, **21**, 19447–19457.

23 M. Li, J. Kłos, A. Petrov and S. Kotochigova, *Communications Physics*, 2019, **2**, 148.

24 M. V. Ivanov, T.-C. Jagau, G.-Z. Zhu, E. R. Hudson and A. I. Krylov, *Physical Chemistry Chemical Physics*, 2020, **22**, 17075–17090.

25 J. Kłos and S. Kotochigova, *Physical Review Research*, 2020, **2**, 013384.

26 B. L. Augenbraun, J. M. Doyle, T. Zelevinsky and I. Kozyryev, *Physical Review X*, 2020, **10**, 031022.

27 C. E. Dickerson, H. Guo, A. J. Shin, B. L. Augenbraun, J. R. Caram, W. C. Campbell and A. N. Alexandrova, *Physical Review Letters*, 2021, **126**, 123002.

28 D. Mitra, Z. D. Lasner, G.-Z. Zhu, C. E. Dickerson, B. L. Augenbraun, A. D. Bailey, A. N. Alexandrova, W. C. Campbell, J. R. Caram, E. R. Hudson and J. M. Doyle, *The Journal of Physical Chemistry Letters*, 2022, **13**, 7029–7035.

29 G.-Z. Zhu, D. Mitra, B. L. Augenbraun, C. E. Dickerson, M. J. Frim, G. Lao, Z. D. Lasner, A. N. Alexandrova, W. C. Campbell, J. R. Caram, J. M. Doyle and E. R. Hudson, *Nature Chemistry*, 2022, **14**, 995–999.

30 M. R. Tarbutt, *Contemporary Physics*, 2019, **59**, 356–376.

31 D. McCarron, *Journal of Physics B: Atomic, Molecular and Optical Physics*, 2018, **51**, 212001.

32 N. J. Fitch and M. R. Tarbutt, *Advances In Atomic, Molecular, and Optical Physics*, Academic Press, 2021, vol. 70, pp. 157–262.

33 J. F. Barry, D. J. McCarron, E. B. Norrgard, M. H. Steinecker and D. DeMille, *Nature*, 2014, **512**, 286–289.

34 D. J. McCarron, E. B. Norrgard, M. H. Steinecker and D. DeMille, *New Journal of Physics*, 2015, **17**, 035014.

35 M. H. Steinecker, D. J. McCarron, Y. Zhu and D. DeMille, *ChemPhysChem*, 2016, **17**, 3664–3669.

36 E. B. Norrgard, D. J. McCarron, M. H. Steinecker, M. R. Tarbutt and D. DeMille, *Physical Review Letters*, 2016, **116**, 063004.

37 T. K. Langin, V. Jorapur, Y. Zhu, Q. Wang and D. DeMille, *Physical Review Letters*, 2021, **127**, 163201.

38 V. Zhelyazkova, A. Cournol, T. E. Wall, A. Matsushima, J. J. Hudson, E. A. Hinds, M. R. Tarbutt and B. E. Sauer, *Physical Review A*, 2014, **89**, 053416.

39 S. Truppe, H. J. Williams, M. Hambach, L. Caldwell, N. J. Fitch, E. A. Hinds, B. E. Sauer and M. R. Tarbutt, *Nature Physics*, 2017, **13**, 1173–1176.

40 L. Anderegg, B. L. Augenbraun, Y. Bao, S. Burchesky, L. W. Cheuk, W. Ketterle and J. M. Doyle, *Nature Physics*, 2018, **14**, 890–893.

41 J. Lim, J. R. Almond, M. A. Trigatzis, J. A. Devlin, N. J. Fitch, B. E. Sauer, M. R. Tarbutt and E. A. Hinds, *Physical Review Letters*, 2018, **120**, 123201.

42 X. Alauze, J. Lim, M. A. Trigatzis, S. Swarbrick, F. J. Collings, N. J. Fitch, B. E. Sauer and M. R. Tarbutt, *Quantum Science and Technology*, 2021, **6**, 044005.

43 R. L. McNally, I. Kozyryev, S. Vazquez-Carson, K. Wenz, T. Wang and T. Zelevinsky, *New Journal of Physics*, 2020, **22**, 083047.

44 R. Albrecht, M. Scharwaechter, T. Sixt, L. Hofer and T. Langen, *Physical Review A*, 2020, **101**, 013413.

45 T. Chen, W. Bu and B. Yan, *Physical Review A*, 2017, **96**, 053401.

46 M. D. Di Rosa, *The European Physical Journal D - Atomic, Molecular, Optical and Plasma Physics*, 2004, **31**, 395–402.

47 L. Baum, N. B. Vilas, C. Hallas, B. L. Augenbraun, S. Raval, D. Mitra and J. M. Doyle, *Physical Review A*, 2021, **103**, 043111.

48 B. K. Stuhl, B. C. Sawyer, D. Wang and J. Ye, *Physical Review Letters*, 2008, **101**, 243002.

49 I. Kozyryev, L. Baum, K. Matsuda, B. L. Augenbraun, L. Anderegg, A. P. Sedlack and J. M. Doyle, *Physical Review Letters*,

2017, **118**, 173201.

50 L. Baum, N. B. Vilas, C. Hallas, B. L. Augenbraun, S. Raval, D. Mitra and J. M. Doyle, *Physical Review Letters*, 2020, **124**, 133201.

51 N. B. Vilas, C. Hallas, L. Anderegg, P. Robichaud, A. Winnicki, D. Mitra and J. M. Doyle, *Nature*, 2022, **606**, 70–74.

52 B. L. Augenbraun, Z. D. Lasner, A. Frenett, H. Sawaoka, C. Miller, T. C. Steimle and J. M. Doyle, *New Journal of Physics*, 2020, **22**, 022003.

53 D. Mitra, N. B. Vilas, C. Hallas, L. Anderegg, B. L. Augenbraun, L. Baum, C. Miller, S. Raval and J. M. Doyle, *Science*, 2020, **369**, 1366–1369.

54 M. Yasuda and H. Katori, *Physical Review Letters*, 2004, **92**, 153004.

55 B. B. Jensen, H. Ming, P. G. Westergaard, K. Gunnarsson, M. H. Madsen, A. Brusch, J. Hald and J. W. Thomsen, *Physical Review Letters*, 2011, **107**, 113001.

56 H. Katori, T. Ido, Y. Isoya and M. Kuwata-Gonokami, *Physical Review Letters*, 1999, **82**, 1116–1119.

57 T. Kuwamoto, K. Honda, Y. Takahashi and T. Yabuzaki, *Physical Review A*, 1999, **60**, R745–R748.

58 T. Binnewies, G. Wilpers, U. Sterr, F. Riehle, J. Helmcke, T. E. Mehlstäubler, E. M. Rasel and W. Ertmer, *Physical Review Letters*, 2001, **87**, 123002.

59 A. Cooper, J. P. Covey, I. S. Madjarov, S. G. Porsev, M. S. Safronova and M. Endres, *Physical Review X*, 2018, **8**, 041055.

60 M. A. Norcia, A. W. Young and A. M. Kaufman, *Physical Review X*, 2018, **8**, 041054.

61 S. Saskin, J. T. Wilson, B. Grinkemeyer and J. D. Thompson, *Physical Review Letters*, 2019, **122**, 143002.

62 W. E. Cooke, T. F. Gallagher, S. A. Edelstein and R. M. Hill, *Physical Review Letters*, 1978, **40**, 178–181.

63 G. Lochead, D. Boddy, D. P. Sadler, C. S. Adams and M. P. A. Jones, *Physical Review A*, 2013, **87**, 053409.

64 I. S. Madjarov, J. P. Covey, A. L. Shaw, J. Choi, A. Kale, A. Cooper, H. Pichler, V. Schkolnik, J. R. Williams and M. Endres, *Nature Physics*, 2020, **16**, 857–861.

65 M. M. Boyd, T. Zelevinsky, A. D. Ludlow, S. Blatt, T. Zanon-Willette, S. M. Foreman and J. Ye, *Physical Review A*, 2007, **76**, 022510.

66 I. Ushijima, M. Takamoto, M. Das, T. Ohkubo and H. Katori, *Nature Photonics*, 2015, **9**, 185–189.

67 S. L. Campbell, R. B. Hutson, G. E. Marti, A. Goban, N. D. Oppong, R. L. McNally, L. Sonderhouse, J. M. Robinson, W. Zhang, B. J. Bloom and J. Ye, *Science*, 2017, **358**, 90–94.

68 M. Takamoto, I. Ushijima, N. Ohmae, T. Yahagi, K. Kokado, H. Shinkai and H. Katori, *Nature Photonics*, 2020, **14**, 411–415.

69 T. Bothwell, C. J. Kennedy, A. Aeppli, D. Kedar, J. M. Robinson, E. Oelker, A. Staron and J. Ye, *Nature*, 2022, **602**, 420–424.

70 I. S. Madjarov, A. Cooper, A. L. Shaw, J. P. Covey, V. Schkolnik, T. H. Yoon, J. R. Williams and M. Endres, *Physical Review X*, 2019, **9**, 041052.

71 A. W. Young, W. J. Eckner, W. R. Milner, D. Kedar, M. A. Norcia, E. Oelker, N. Schine, J. Ye and A. M. Kaufman, *Nature*, 2020, **588**, 408–413.

72 A. V. Gorshkov, M. Hermele, V. Gurarie, C. Xu, P. S. Julienne, J. Ye, P. Zoller, E. Demler, M. D. Lukin and A. M. Rey, *Nature Physics*, 2010, **6**, 289–295.

73 S. Taie, R. Yamazaki, S. Sugawa and Y. Takahashi, *Nature Physics*, 2012, **8**, 825–830.

74 C. Hofrichter, L. Riegger, F. Scazza, M. Hofer, D. R. Fernandes, I. Bloch and S. Folling, *Physical Review X*, 2016, **6**, 021030.

75 H. Ozawa, S. Taie, Y. Takasu and Y. Takahashi, *Physical Review Letters*, 2018, **121**, 225303.

76 L. Sonderhouse, C. Sanner, R. B. Hutson, A. Goban, T. Bilitewski, L. Yan, W. R. Milner, A. M. Rey and J. Ye, *Nature Physics*, 2020, **16**, 1216–1221.

77 F. Schäfer, T. Fukuhara, S. Sugawa, Y. Takasu and Y. Takahashi, *Nature Reviews Physics*, 2020, **2**, 411–425.

78 J. Rudolph, T. Wilkason, M. Nantel, H. Swan, C. M. Holland, Y. Jiang, B. E. Garber, S. P. Carman and J. M. Hogan, *Physical Review Letters*, 2020, **124**, 083604.

79 G. Pagano, F. Scazza and M. Foss-Feig, *Advanced Quantum Technologies*, 2019, **2**, 1800067.

80 A. J. Daley, M. M. Boyd, J. Ye and P. Zoller, *Physical Review Letters*, 2008, **101**, 170504.

81 J. P. Covey, A. Sipahigil, S. Szoke, N. Sinclair, M. Endres and O. Painter, *Physical Review Applied*, 2019, **11**, 034044.

82 A. V. Gorshkov, A. M. Rey, A. J. Daley, M. M. Boyd, J. Ye, P. Zoller and M. D. Lukin, *Physical Review Letters*, 2009, **102**, 110503.

83 A. Jenkins, J. W. Lis, A. Senoo, W. F. McGrew and A. M. Kaufman, *Physical Review X*, 2022, **12**, 021027.

84 S. Ma, A. P. Burgers, G. Liu, J. Wilson, B. Zhang and J. D. Thompson, *Physical Review X*, 2022, **12**, 021028.

85 K. Barnes, P. Battaglino, B. J. Bloom, K. Cassella, R. Coxe, N. Crisosto, J. P. King, S. S. Kondov, K. Kotru, S. C. Larsen, J. Lauigan, B. J. Lester, M. McDonald, E. Megidish, S. Narayanaswami, C. Nishiguchi, R. Notermans, L. S. Peng, A. Ryou, T.-Y. Wu and M. Yarwood, *Nature Communications*, 2022, **13**, 2779.

86 S. Truppe, S. Marx, S. Kray, M. Doppelbauer, S. Hofsäss, H. C. Schewe, N. Walter, J. Pérez-Ríos, B. G. Sartakov and G. Meijer, *Physical Review A*, 2019, **100**, 052513.

87 S. Hofsäss, M. Doppelbauer, S. Wright, S. Kray, B. Sartakov, J. Pérez-Ríos, G. Meijer and S. Truppe, *New Journal of Physics*, 2021, **23**, 075001.

88 J. R. Daniel, C. Wang, K. Rodriguez, B. Hemmerling, T. N. Lewis, C. Bardeen, A. Teplukhin and B. K. Kendrick, *Physical Review A*, 2021, **104**, 012801.

89 L. R. Hunter, S. K. Peck, A. S. Greenspon, S. S. Alam and D. DeMille, *Physical Review A*, 2012, **85**, 012511.

90 E. B. Norrgard, E. R. Edwards, D. J. McCarron, M. H. Stei-

necker, D. DeMille, S. S. Alam, S. K. Peck, N. S. Wadia and L. R. Hunter, *Physical Review A*, 2017, **95**, 062506.
91 N. Wells and I. C. Lane, *Physical Chemistry Chemical Physics*, 2011, **13**, 19018–19025.
92 Y.-f. Gao and T. Gao, *Physical Chemistry Chemical Physics*, 2015, **17**, 10830–10837.
93 M. Wan, D. Yuan, C. Jin, F. Wang, Y. Yang, Y. Yu and J. Shao, *The Journal of Chemical Physics*, 2016, **145**, 024309.
94 R. Yang, B. Tang and T. Gao, *Chinese Physics B*, 2016, **25**, 043101.
95 Y. Gao and M. Wan, *Physical Chemistry Chemical Physics*, 2017, **19**, 5519–5524.
96 Y.-G. Zhang, H. Zhang, H.-Y. Song, Y. Yu and M.-J. Wan, *Physical Chemistry Chemical Physics*, 2017, **19**, 24647–24655.
97 X. Yuan, S. Yin, Y. Shen, Y. Liu, Y. Lian, H.-F. Xu and B. Yan, *The Journal of Chemical Physics*, 2018, **149**, 094306.
98 X. Y. Ren, Z. Y. Xiao, Y. Liu and B. Yan, *Chinese Physics B*, 2021, **30**, 053101.
99 W. Xia, M. Fu, H. Ma and W. Bian, *Chemical Physics*, 2017, **485–486**, 29–34.
100 Y.-G. Zhang, G. Dou, J.-X. Qi and J. Cui, *Computational and Theoretical Chemistry*, 2018, **1134**, 8–14.
101 D. Li, M. Fu, H. Ma, W. Bian, Z. Du and C. Chen, *Frontiers in Chemistry*, 2020, **8**, 20.
102 P. Yu and N. R. Hutzler, *Physical Review Letters*, 2021, **126**, 023003.
103 M. L. Wall, K. Maeda and L. D. Carr, *Annalen der Physik*, 2013, **525**, 845–865.
104 M. L. Wall, K. Maeda and L. D. Carr, *New Journal of Physics*, 2015, **17**, 025001.
105 R. Mitra, V. S. Prasannaa, B. K. Sahoo, N. R. Hutzler, M. Abe and B. P. Das, *Atoms*, 2021, **9**, 7.
106 S. Chu, *Rev. Mod. Phys.*, 1998, **70**, 685.
107 I. Kozyryev, L. Baum, K. Matsuda, B. Hemmerling and J. M. Doyle, *J. Phys. B: At. Mol. Opt. Phys.*, 2016, **49**, 134002.
108 I. Kozyryev, L. Baum, L. Aldridge, P. Yu, E. E. Eyler and J. M. Doyle, *Physical Review Letters*, 2018, **120**, 063205.
109 E. R. Hudson, J. R. Bochinski, H. J. Lewandowski, B. C. Sawyer and J. Ye, *The European Physical Journal D - Atomic, Molecular, Optical and Plasma Physics*, 2004, **31**, 351–358.
110 B. C. Sawyer, B. L. Lev, E. R. Hudson, B. K. Stuhl, M. Lara, J. L. Bohn and J. Ye, *Physical Review Letters*, 2007, **98**, 253002.
111 E. R. Hudson, *Physical Review A*, 2009, **79**, 061407(R).
112 M. Petzold, P. Kaebert, P. Gersema, M. Siercke and S. Ospelkaus, *New Journal of Physics*, 2018, **20**, 042001.
113 P. Aggarwal, Y. Yin, K. Esajas, H. L. Bethlem, A. Boeschoten, A. Borschevsky, S. Hoekstra, K. Jungmann, V. R. Marshall, T. B. Meijknecht, M. C. Mooij, R. G. E. Timmermans, A. Touwen, W. Ubachs and L. Willmann, *Physical Review Letters*, 2021, **127**, 173201.
114 M. Zeppenfeld, B. G. U. Englert, R. Glöckner, A. Prehn, M. Mielenz, C. Sommer, L. D. van Buuren, M. Motsch and G. Rempe, *Nature*, 2012, **491**, 570–573.
115 A. Prehn, M. Ibrügger, R. Glöckner, G. Rempe and M. Zeppenfeld, *Physical Review Letters*, 2016, **116**, 063005.
116 N. J. Fitch and M. R. Tarbutt, *ChemPhysChem*, 2016, **17**, 3609–3623.
117 B. L. Augenbraun, A. Frenett, H. Sawaoka, C. Hallas, N. B. Vilas, A. Nasir, Z. D. Lasner and J. M. Doyle, *Physical Review Letters*, 2021, **127**, 263002.
118 H. Sawaoka, A. Frenett, A. Nasir, T. Ono, B. L. Augenbraun, T. C. Steimle and J. M. Doyle, *Zeeman-Sisyphus Deceleration for Heavy Molecules with Perturbed Excited-State Structure, arXiv:2210.10859*, 2022.
119 H.-I. Lu, I. Kozyryev, B. Hemmerling, J. Piskorski and J. M. Doyle, *Physical Review Letters*, 2014, **112**, 113006.
120 T. J. Lee and G. E. Scuseria, *Quantum Mechanical Electronic Structure Calculations with Chemical Accuracy*, Springer Netherlands, Dordrecht, 1995, pp. 47–108.
121 A. I. Krylov, *Annual Review of Physical Chemistry*, 2008, **59**, 433–462.
122 E. T. Mengesha, A. T. Le, T. C. Steimle, L. Cheng, C. Zhang, B. L. Augenbraun, Z. Lasner and J. Doyle, *The Journal of Physical Chemistry A*, 2020, **124**, 3135–3148.
123 C. Zhang, B. L. Augenbraun, Z. D. Lasner, N. B. Vilas, J. M. Doyle and L. Cheng, *The Journal of Chemical Physics*, 2021, **155**, 091101.
124 C. Zhang, C. Zhang, L. Cheng, T. C. Steimle and M. R. Tarbutt, *Journal of Molecular Spectroscopy*, 2022, **386**, 111625.
125 Z. Lasner, A. Lunstad, C. Zhang, L. Cheng and J. M. Doyle, *Physical Review A*, 2022, **106**, L020801.
126 J. F. Stanton and R. J. Bartlett, *The Journal of Chemical Physics*, 1993, **98**, 7029–7039.
127 A. I. Krylov, *Chemical Physics Letters*, 2001, **338**, 375–384.
128 A. I. Krylov, *Accounts of Chemical Research*, 2006, **39**, 83–91.
129 E. Epifanovsky *et al.*, *The Journal of Chemical Physics*, 2021, **155**, 084801.
130 F. Plasser, M. Wormit and A. Dreuw, *The Journal of Chemical Physics*, 2014, **141**, 024106.
131 S. Gozem and A. I. Krylov, *WIREs Computational Molecular Science*, 2021, **12**, e1546.
132 D. E. Woon and T. H. Dunning, *The Journal of Chemical Physics*, 1993, **98**, 1358–1371.
133 A. K. Wilson, D. E. Woon, K. A. Peterson and T. H. Dunning, *The Journal of Chemical Physics*, 1999, **110**, 7667–7676.
134 K. A. Peterson, *The Journal of Chemical Physics*, 2003, **119**, 11099–11112.
135 B. Metz, M. Schweizer, H. Stoll, M. Dolg and W. Liu, *Theoretical Chemistry Accounts: Theory, Computation, and Modeling (Theoretica Chimica Acta)*, 2000, **104**, 22–28.
136 B. Metz, H. Stoll and M. Dolg, *The Journal of Chemical Physics*, 2000, **113**, 2563–2569.
137 G. Knizia, *Journal of Chemical Theory and Computation*, 2013, **9**, 4834–4843.
138 A. E. Reed, R. B. Weinstock and F. Weinhold, *The Journal of Chemical Physics*, 1985, **83**, 735–746.

139 E. D. Glendening, J. K. Badenhoop, A. E. Reed, J. E. Carpenter, J. A. Bohmann, C. M. Morales and F. Weinhold, *NBO 5.0*, Theoretical Chemistry Institute, University of Wisconsin, 2001.

140 U. C. Singh and P. A. Kollman, *Journal of Computational Chemistry*, 1984, **5**, 129–145.

141 B. H. Besler, K. M. Merz Jr. and P. A. Kollman, *Journal of Computational Chemistry*, 1990, **11**, 431–439.

142 C. M. Breneman and K. B. Wiberg, *Journal of Computational Chemistry*, 1990, **11**, 361–373.

143 P. Pokhilko, R. Shannon, D. Glowacki, H. Wang and A. I. Krylov, *The Journal of Physical Chemistry A*, 2019, **123**, 482–491.

144 P. Pokhilko, E. Epifanovsky and A. I. Krylov, *The Journal of Chemical Physics*, 2019, **151**, 034106.

145 E. Epifanovsky, K. Klein, S. Stopkowicz, J. Gauss and A. I. Krylov, *The Journal of Chemical Physics*, 2015, **143**, 064102.

146 J. P. Zobel, P.-O. Widmark and V. Veryazov, *Journal of Chemical Theory and Computation*, 2020, **16**, 278–294.

147 L. Cheng, F. Wang, J. F. Stanton and J. Gauss, *The Journal of Chemical Physics*, 2018, **148**, 044108.

148 W. A. Goddard and L. B. Harding, *Annual Review of Physical Chemistry*, 1978, **29**, 363–396.

149 P.-O. Löwdin, *Reviews of Modern Physics*, 1962, **34**, 80–87.

150 V. Weisskopf and E. Wigner, *Zeitschrift für Physik*, 1930, **63**, 54–73.

151 M. O. Scully and M. S. Zubairy, *Quantum Optics*, Cambridge University Press, 1st edn, 1997.

152 A. C. Paul, K. Sharma, M. A. Reza, H. Telfah, T. A. Miller and J. Liu, *The Journal of Chemical Physics*, 2019, **151**, 134303.

153 F. J. Grieman, A. T. Droege and P. C. Engelking, *The Journal of Chemical Physics*, 1983, **78**, 2248–2253.

154 R. D. Verma, *Canadian Journal of Physics*, 1962, **40**, 586–597.

155 R. W. Martin and A. J. Merer, *Canadian Journal of Physics*, 1973, **51**, 634–643.

156 R. W. Martin and A. J. Merer, *Canadian Journal of Physics*, 1973, **51**, 125–143.

157 T. A. Isaev, A. V. Zaitsevskii and E. Eliav, *Journal of Physics B: Atomic, Molecular and Optical Physics*, 2017, **50**, 225101.

158 M. V. Ivanov, F. H. Bangerter, P. Wójcik and A. I. Krylov, *The Journal of Physical Chemistry Letters*, 2020, **11**, 6670–6676.

159 I. Kozyryev, T. C. Steimle, P. Yu, D.-T. Nguyen and J. M. Doyle, *New Journal of Physics*, 2019, **21**, 052002.

160 B. L. Augenbraun, Z. D. Lasner, A. Frenett, H. Sawaoka, A. T. Le, J. M. Doyle and T. C. Steimle, *Physical Review A*, 2021, **103**, 022814.

161 A. C. Paul, K. Sharma, H. Telfah, T. A. Miller and J. Liu, *The Journal of Chemical Physics*, 2021, **155**, 024301.

162 G. M. Greetham and A. M. Ellis, *Journal of Chemical Physics*, 2000, **113**, 8945–8952.

163 R. Essers, J. Tennyson and P. E. S. Wormer, *Chemical Physics Letters*, 1982, **89**, 223–227.

164 Y. Ni, *PhD thesis*, University of California Santa Barbara, 1986.

165 W. L. Barclay, M. A. Anderson and L. M. Ziurys, *Chemical Physics Letters*, 1992, **196**, 225–232.

166 A. J. Apponi, W. L. Barclay, Jr. and L. M. Ziurys, *The Astrophysical Journal Letters*, 1993, **414**, L129–L132.

167 J. S. Pilgrim, D. L. Robbins and M. A. Duncan, *Chemical Physics Letters*, 1993, **202**, 203–208.

168 T. Trabelsi and J. S. Francisco, *The Astrophysical Journal*, 2018, **863**, 139.

169 G. Vacek, B. J. DeLeeuw and H. F. Schaefer, *The Journal of Chemical Physics*, 1993, **98**, 8704–8709.

170 S. Li, K. W. Sattelmeyer, Y. Yamaguchi and H. F. Schaefer, *The Journal of Chemical Physics*, 2003, **119**, 12830–12841.

171 E. Hirota, *High-Resolution Spectroscopy of Transient Molecules*, Springer-Verlag, Berlin, 1985, vol. 40.

172 L. Salem and C. Rowland, *Angewandte Chemie International Edition in English*, 1972, **11**, 92–111.

173 S. Shaik and N. D. Epiotis, *Journal of the American Chemical Society*, 1978, **100**, 18–29.

174 C. Doubleday, J. W. McIver and M. Page, *Journal of the American Chemical Society*, 1982, **104**, 6533–6542.

175 L. Carlacci, C. Doubleday, T. R. Furlani, H. F. King and J. W. McIver, *Journal of the American Chemical Society*, 1987, **109**, 5323–5329.

176 N. R. Hutzler, H.-I. Lu and J. M. Doyle, *Chemical Reviews*, 2012, **112**, 4803–4827.

177 E. Kagi and K. Kawaguchi, *The Astrophysical Journal*, 1997, **491**, L128.

178 A. Janczyk and L. M. Ziurys, *Chemical Physics Letters*, 2002, **365**, 514–524.

179 M. P. Bucchino, P. M. Sheridan, J. P. Young, M. K. L. Binns, D. W. Ewing and L. M. Ziurys, *The Journal of Chemical Physics*, 2013, **139**, 214307.

180 C. N. Jarman and P. F. Bernath, *The Journal of Chemical Physics*, 1993, **98**, 6697–6703.

181 P. M. Sheridan, M. J. Dick, J.-G. Wang and P. F. Bernath, *Molecular Physics*, 2007, **105**, 569–583.

182 A. Taleb-Bendiab and D. Chomiak, *Chemical Physics Letters*, 2001, **334**, 195–199.

183 C. T. Scurlock, T. Henderson, S. Bosely, K. Y. Jung and T. C. Steimle, *The Journal of Chemical Physics*, 1994, **100**, 5481–5490.

184 T. Okabayashi, T. Yamamoto, D.-i. Mizuguchi, E. Y. Okabayashi and M. Tanimoto, *Chemical Physics Letters*, 2012, **551**, 26–30.

185 M. P. Bucchino, G. R. Adande, D. T. Halfen and L. M. Ziurys, *The Journal of Chemical Physics*, 2017, **147**, 154313.

186 A. Janczyk and L. M. Ziurys, *The Astrophysical Journal*, 2006, **639**, L107–L110.

187 P. Crozet, F. Martin, A. J. Ross, C. Linton, M. J. Dick and A. G. Adam, *Journal of Molecular Spectroscopy*, 2002, **213**, 28–34.

188 C. J. Whitham, S. A. Beaton, Y. Ito and J. M. Brown, *Journal of Molecular Spectroscopy*, 1998, **191**, 286–294.

189 K.-i. C. Namiki, J. S. Robinson and T. C. Steimle, *J. Chem. Phys.*, 1998, **109**, 5283.

190 M. Elhanine, R. Lawruszczuk and B. Soep, *Chemical Physics Letters*, 1998, **288**, 785–792.

191 A. C. Paul, M. A. Reza and J. Liu, *Journal of Molecular Spectroscopy*, 2016, **330**, 142–146.

192 A. Jadbabaie, N. H. Pilgram, J. Klos, S. Kotochigova and N. R. Hutzler, *New Journal of Physics*, 2020, **22**, 022002.

193 N. H. Pilgram, A. Jadbabaie, Y. Zeng, N. R. Hutzler and T. C. Steimle, *The Journal of Chemical Physics*, 2021, **154**, 244309.

194 W. C. Campbell, E. Tsikata, H.-I. Lu, L. D. van Buuren and J. M. Doyle, *Physical Review Letters*, 2007, **98**, 213001.

195 J. D. Weinstein, R. deCarvalho, T. Guillet, B. Friedrich and J. M. Doyle, *Nature*, 1998, **395**, 148–150.

196 H. Metcalf, *Reviews of Modern Physics*, 2017, **89**, 041001.

197 M. A. Chieda and E. E. Eyler, *Physical Review A*, 2011, **84**, 063401.

198 L. Aldridge, S. E. Galica and E. E. Eyler, *Physical Review A*, 2016, **93**, 013419.

199 S. E. Galica, L. Aldridge, D. J. McCarron, E. E. Eyler and P. L. Gould, *Physical Review A*, 2018, **98**, 023408.

200 K. Wenz, I. Kozyryev, R. L. McNally, L. Aldridge and T. Zelevinsky, *Physical Review Research*, 2020, **2**, 043377.

201 A. M. Jayich, A. C. Vutha, M. T. Hummon, J. V. Porto and W. C. Campbell, *Physical Review A*, 2014, **89**, 023425.

202 X. Long, S. S. Yu, A. M. Jayich and W. C. Campbell, *Physical Review Letters*, 2019, **123**, 033603.

203 E. A. Curtis, C. W. Oates and L. Hollberg, *Physical Review A*, 2001, **64**, 031403(R).

204 N. Rehbein, T. E. Mehlstäubler, J. Keupp, K. Moldenhauer, E. M. Rasel, W. Ertmer, A. Douillet, V. Michels, S. G. Porsev, A. Derevianko, C. Froese Fischer, G. I. Tachiev and V. G. Pal'chikov, *Physical Review A*, 2007, **76**, 043406.

205 P. Rabl, D. DeMille, J. M. Doyle, M. D. Lukin, R. J. Schoelkopf and P. Zoller, *Physical Review Letters*, 2006, **97**, 033003.

206 J. W. Park, Z. Z. Yan, H. Loh, S. A. Will and M. W. Zwierlein, *Science*, 2017, **375**, 372–375.

207 R. Zhang, Y. Cheng, H. Zhai and P. Zhang, *Physical Review Letters*, 2015, **115**, 135301.

208 R. Zhang, Y. Cheng, P. Zhang and H. Zhai, *Nature Reviews Physics*, 2020, **2**, 213–220.

209 V. Galitski and I. B. Spielman, *Nature*, 2013, **494**, 49–54.

210 L. F. Livi, G. Cappellini, M. Diem, L. Franchi, C. Clivati, M. Frittelli, F. Levi, D. Calonico, J. Catani, M. Inguscio and L. Fallani, *Physical Review Letters*, 2016, **117**, 220401.

211 M. L. Wall, A. P. Koller, S. Li, X. Zhang, N. R. Cooper, J. Ye and A. M. Rey, *Physical Review Letters*, 2016, **116**, 035301.

212 S. Kolkowitz, S. L. Bromley, T. Bothwell, M. L. Wall, G. E. Marti, A. P. Koller, X. Zhang, A. M. Rey and J. Ye, *Nature*, 2017, **542**, 66–70.

213 S. L. Bromley, S. Kolkowitz, T. Bothwell, D. Kedar, A. Safavi-Naini, M. L. Wall, C. Salomon, A. M. Rey and J. Ye, *Nature Physics*, 2018, **14**, 399–404.

214 M. L. Wall, K. R. A. Hazzard and A. M. Rey, *From Atomic To Mesoscale: The Role of Quantum Coherence in Systems of Various Complexities*, World Scientific Publishing, Hackensack, NJ, 2015, pp. 3–37.

215 T. E. Chupp, P. Fierlinger, M. J. Ramsey-Musolf and J. T. Singh, *Reviews of Modern Physics*, 2019, **91**, 015001.

216 M. S. Safronova, D. Budker, D. Demille, D. F. J. Kimball, A. Derevianko and C. W. Clark, *Reviews of Modern Physics*, 2018, **90**, 25008.

217 K. I. Baklanov, A. N. Petrov, A. V. Titov and M. G. Kozlov, *Physical Review A*, 2010, **82**, 060501(R).

218 M. G. Kozlov and D. DeMille, *Physical Review Letters*, 2002, **89**, 133001.

219 V. A. Dzuba, V. V. Flambaum, J. S. M. Ginges and M. G. Kozlov, *Physical Review A*, 2002, **66**, 012111.

220 V. S. Prasannaa, A. C. Vutha, M. Abe and B. P. Das, *Physical Review Letters*, 2015, **114**, 183001.

221 H. Hergert, *Frontiers in Physics*, 2020, **8**, 379.

222 Ronald Garcia Ruiz, *(Private Communication)*.

223 Jason Holt, *(Private Communication)*.

224 A. V. Kudrin, A. Zaitsevskii, T. A. Isaev, D. E. Maison and L. V. Skripnikov, *Atoms*, 2019, **7**, 62.

225 C. E. Dickerson, H. Guo, G.-Z. Zhu, E. R. Hudson, J. R. Caram, W. C. Campbell and A. N. Alexandrova, *The Journal of Physical Chemistry Letters*, 2021, **12**, 3989–3995.